Strain localization and fluid infiltration in the mantle wedge during subduction initiation: Evidence from the base of the New Caledonia ophiolite

Mathieu Soret, Philippe Agard, Benoît Dubacq, A. Vitale-Brovarone, Patrick Monie, Alain Chauvet, H. Whitechurch, Benoît Villemant

Strain localization and fluid infiltration in the mantle wedge during subduction initiation: evidence from the base of the New Caledonia ophiolite

M. Soret[1], P. Agard[1,2], B. Dubacq[1], A. Vitale-Brovarone[3], P. Monié[4], A. Chauvet[4], H. Whitechurch[5], B. Villemant[1]

[1] *Sorbonne Universités, UPMC Univ Paris 06, CNRS, Institut des Sciences de la Terre de Paris (ISTeP), 4 place Jussieu 75005 Paris, France*

[2]*Insitut Universitaire de France, F-75005, Paris, France*

[3] *Institut de Minéralogie, de Physique des Matériaux, et de Cosmochimie, Sorbonne Universités, UMR CNRS 7590, Université Pierre et Marie Curie Paris 06, Muséum National d'Histoire Naturelle, Institut de Recherche pour le Développement UMR 206, 4 place Jussieu, 75005 Paris, France.*

[4]*Université Montpellier 2, Géosciences Montpellier, UMR CNRS 5243, Place E. Bataillon, 34095, Montpellier Cedex 05, France.*

[5]*IPGS, Université de Strasbourg, UMR CNRS 7516; 1, rue Blessig, 67000 Strasbourg, France*

Abstract

Despite decades of petrological and geochemical studies, the nature and setting of obducted ophiolites remain controversial: the influence of supra-subduction zone environments on pre-existing oceanic lithosphere is yet to assess, and the processes leading to subduction/obduction initiation are still poorly constrained. Our study documents successive influx of slab-derived fluids and progressive strain localization within the upper mantle in a supra-subduction environment during the first few My of the subduction history. We focus on strongly sheared mafic amphibolites intruding peridotites near the mantle–crust transition of the New Caledonia obducted ophiolite and ~50 to 100 m above the basal thrust contact of the ophiolite. These m- to hm-long and several m-thick shear bands are interpreted as inherited small-scale intrusions of mafic melts, probably dikes or sills, which were derived from a moderately refractory mantle source refertilized by supra-subduction zone fluids. $^{40}Ar/^{39}Ar$ age constraints on pargasite at ca. 90 Ma suggest that they could be inherited from the former Pacific west-dipping subduction.

Secondary deformation of these mafic intrusions is intimately associated to three major stages of fluid infiltration: (1) the first stage of deformation and metasomatism is marked by syn-kinematic growth of Ca-amphibole (at 700–800 ºC and 3–5 kbar) with a distinctive supra-subduction zone signature, and controlled later channelization of aqueous fluids. $^{40}Ar/^{39}Ar$ dating on magnesio-hornblende indicates that this deformation episode occurred at ca. 55 Ma, coincident with east-dipping subduction initiation; (2) the main metasomatic stage, characterized by the development of a phlogopite-rich matrix wrapping peridotites and amphibolite boudins, points to the percolation of alkali-rich aqueous fluids at still high

47 temperature (650–750 ºC); (3) the last, low temperature (< 600 ºC) metasomatic stage
48 results in the formation of deformed veinlets containing talc, chlorite and serpentine.
49

50 1. Introduction

51 Obduction emplaces fragments of dense oceanic lithosphere on top of
52 continents over several hundreds of kilometers (e.g. Oman, Newfoundland, Turkey,
53 New Caledonia; Coleman, 1971). Despite numerous petrological and geochemical
54 studies, the exact nature and setting of many obducted ophiolites remain unclear. The
55 Oman ophiolite is a typical example where there are evidences for both a MORB-type
56 signature (Boudier et al., 1988; Ceuleneer et al., 1988; Nicolas et al., 2000; Godard et
57 al., 2000, 2003; Le Mée et al., 2004) and a supra-subduction zone (SSZ) geochemical
58 imprint (Ernewein &al, 1988, Stern and Bloomer, 1992; Shervais, 2001; McLeod et
59 al., 2013).

60 The origin of obducted ophiolites has long been debated (Coleman, 1971,
61 Dewey and Bird, 1971; Nicolas, 1989; Moores et al., 2000), with recent studies
62 focusing on subduction-obduction initiation and early emplacement of ophiolites
63 (Vaughan and Scarrow, 2003; Agard et al., 2007, 2014; Lagabrielle et al., 2013).
64 Most of our knowledge on the initiation of the subduction-obduction system comes
65 from the amphibolite to granulite facies metamorphic soles found at the base of most
66 large-scale non-metamorphosed ophiolites and from magmatic dikes emplaced at
67 different levels of the mantle sequence. These dikes generally record partial
68 refertilization of the mantle wedge by subduction-derived fluids and show little
69 deformation (e.g. Pirard, 2012; Xiong et al., 2014) whereas metamorphic soles are
70 highly deformed portions of upper oceanic crust and sediments, heated and

metamorphosed along the interface between the subducting slab and the hotter mantle wedge during early subduction (e.g. Wakabayashi and Dilek, 2003). Metamorphic soles typically predate the final emplacement of the ophiolite onto the continental margin by several millions of years (~20 My for Oman; Agard et al., 2007).

We document sheared mafic amphibolite and feldspar-rich veins outcropping over a scale of hundreds of meters, within the peridotites of the New Caledonia ophiolite. They occur near the crust–mantle transition zone (e.g. Prinzhofer et al., 1980; Pirard et al., 2013) and ~50 to 100 m above the basal contact of the ophiolite, south east of Noumea (Fig.1). As these deformed, metamorphosed rocks occur at the base of the New Caledonia ophiolite, it is tempting to relate them to subduction initiation, as for metamorphic soles. These sheared amphibolites could represent metamorphic sole fragments (outcropping in the Thio area; Cluzel et al., 2001, 2012) tectonically imbricated with basal peridotites, or be derived from melt products triggered by subduction-derived fluids (e.g. as the SSZ amphibole-bearing dikes in the Massif du Sud peridotites; Cluzel et al., 2006; Pirard, 2012; Pirard et al., 2013). Alternatively, they could also be inherited from earlier melting processes during ocean basin formation (e.g. near transform fault; Gaggero and Cortesogno, 1997; Constantin, 1999).

In this study, we provide a detailed petrological, geochemical and geochronological study to constrain the nature, the tectonic setting and the origin of these deformed amphibole-bearing dikes, and discuss implications for the New Caledonia subduction system in terms of geological setting and refertilization.

2. Geological setting

New Caledonia is located at the northern termination of the Norfolk Ridge, a stretched continental fragment rifted off the eastern Australian margin during the Early Cretaceous rollback of the Western Pacific subduction zone and the opening of New Caledonia and Loyalty basins (Weissel and Hayes, 1977; Van de Beuque et al., 1998; Schellart et al. 2006).

The present-day structure of New Caledonia (Fig. 1a) results from a Paleogene episode of convergence. This event led to the closure of the South Loyalty Basin after the initiation of a north-east-dipping intra-oceanic subduction (Cluzel et al., 2001; Schellart et al., 2006; Matthews et al., 2015) and was responsible for the obduction of the New Caledonia ophiolite rooted in the Loyalty Basin (Collot et al., 1987). Geochronological and thermochronological data on mafic rocks from the metamorphic sole (Cluzel et al. 2012) and mafic dikes intruding the ultramafic ophiolite (Cluzel et al. 2006; Pirard, 2012) suggest that subduction inception occurred at ca. 56 Ma. At ca. 34 Ma, this intra-oceanic subduction led to the obduction of the South Loyalty Basin lithosphere toward the south-west onto the Norfolk Ridge (e.g. Paris, 1979; Prinzhofer, 1981; Collot et al., 1987).

The ophiolite complex of New Caledonia is composed of three allochtonous units of Cretaceous–Eocene age accreted over a calc-alkaline, island-arc derived basement (Fig.1a) (Aitchison et al., 1995; Cluzel et al., 2001). This basement was created from the Permian to the Early Cretaceous with the accretion of three major volcano-sedimentary terranes (i.e. Teremba, Boghen and Koh terranes) along the eastern Gondwana margin. Above this basement, the Tertiary subduction complex is composed of four main units:

1 — a Tertiary high-pressure metamorphic belt at the northern end of New-Caledonia (Fig.1a) made of volcano-sedimentary and mafic blueschist and eclogite facies rocks, some of which are interbedded in a serpentinite matrix and minor metasediments (Clarke et al., 1997; Carson et al., 2000; Cluzel et al., 2001; Vitale-Brovarone and Agard, 2013). Mafic eclogites have Late Cretaceous to Eocene protolith ages and share geochemical affinities with the Poya terrane (Cluzel et al., 2001; Spandler et al., 2005)

2 — the Poya terrane, a weakly metamorphic mafic rocks unit (e.g. Eissen et al., 1998; Cluzel et al., 1997, 2001), outcrops along most of the west coast of New Caledonia and also forms several isolated exposures along the eastern side (Fig.1a). This terrane consists mainly of massive and pillow basalt, dolerite, and gabbro associated with chert and volcaniclastic rocks (Eissen et al., 1998). The origin of the Poya Terrane is controversial. Geochemical associations of back-arc basin and enriched-MORB signatures constrain its formation to a back-arc environment (Cluzel et al., 1997, 2001). Paleontological studies date its formation between 83 and 55 Ma (Cluzel et al., 2001). This unit was interpreted as representing the crustal cover of the South Loyalty Basin (Spandler et al., 2005; Lagabrielle et al., 2013), with the above ages likely indicating the opening period of the basin.

3 — the ultramafic ophiolite (named “Nappe des Péridotites”) found on the south-eastern portion of New Caledonia (Fig.1a) is constituted mainly of a 2–3 km thick depleted mantle sequence (spinel-bearing harzburgite) above a 20 to 100 m thick porphyroclastic serpentine mylonite. In the northern part of New Caledonia, lherzolite is present in the Tiebaghi and the Poum massifs (e.g. Moutte, 1979; Ulrich et al., 2010). This suite of ultramafic rocks is interpreted as representing upper mantle rocks of the South Loyalty Basin (Lagabrielle et al., 2013) and documents a complex

history with several supra-subduction zone settings, as attested by magmatic intrusions.

In the Massif du Sud, Marchesi et al. (2009) and Pirard et al. (2013) reported gabbronorites and olivine gabbro sills at the top of ophiolitic sequence. These gabbros represent the lower crust of the ophiolite. They are separated from the underlying harzburgite by a dunite complex composed of dunite channels with the presence of dunite cumulates, wherlite, clinopyroxenite and websterite sills and dikes. Amphibole is commonly present in clinopyroxenite bodies but absent from the lower crust gabbronorites (Pirard, 2012; Pirard et al., 2013). These authors interpret this complex as the crust–mantle transition with mafic sills and dikes being the result of percolating, hydrous primitive arc magmas within the peridotite during early stages of the subduction system and nascent arc crust formation.

The Massif du Sud is also extensively cross-cut by Early Eocene felsic, anhydrous and hydrous coarse grained dikes (leucodiorite, granitoid, micro-diorite, dolerite and hornblendite; Prinzhofer, 1981; Cluzel et al., 2005, 2006; Pirard, 2012; Pirard et al., 2013) discordant with the harzburgite and/or the gabbro sills from the lower crust. These dikes are generally unmetamorphosed and undeformed with the exception of few diorite dikes which are boudinaged, locally micro-folded and where amphibole shows a preferred orientation (Cluzel et al., 2012). Upon geochemical and geochronological features, these dikes have been interpreted as formed in a supra-subduction zone setting. These dikes are essentially considered as synchronous or immediately posterior to magma injection in active faults that formed during the first stages of the 55 Ma subduction (Cluzel et al., 2006, 2012). However, Prinzhofer (1981) obtained 2 different K-Ar ages (i.e. 90 ± 10 Ma and 42 ± 5 Ma) for dolerite dikes intruding the Massif du Sud. The youngest dikes coincide with the Eocene New

Caledonia subduction. The Late Cretaceous dikes could be an evidence of the ocean spreading stage of the South Loyalty Basin (Prinzhofer, 1981; Matthews et al., 2015). The Late Cretaceous age of 85 Ma was also measured in zircon cores from the high-pressure Pouebo unit (Spandler et al., 2005). In addition, Cluzel et al. (2005) report granitoid dikes intruding the Massif du Sud at 27 and 24 Ma. They interpret these dikes, coeval with the final obduction stages, as related to the inception of a new subduction along the west coast of New Caledonia in response to the blocking of the previous Eocene subduction. Altogether these dikes appear to record several subduction-related events, suggesting that the ophiolite witnesses several and distinctive stages of migration, accumulation and re-equilibration of different melts (including hydrous melts) in a supra-subduction environment (e.g. Marchesi et al., 2009; Ulrich et al., 2010; Pirard, 2012), rather than being the result of a fractional crystallization from a single magma-type during oceanic spreading (Prinzhofer and Allègre, 1985).

4 — an amphibolite to granulite facies metamorphic sole is found in places between the ophiolite and the Poya and Pouebo underlying terranes (Cluzel et al., 2012). This metamorphic sole is interpreted to have been welded to the ophiolite during subduction inception. Using various thermobarometers, Cluzel et al. (2012) estimate peak crystallization conditions around 5 kbar and 800 to 950 °C. Thermochronology on hornblende ($^{40}Ar/^{39}Ar$), zircon and sphene (U-Pb) indicate that these mafic rocks crystallized at ca. 56 Ma (Cluzel et al., 2012). This result and inferred pressure–temperature conditions for the New Caledonia metamorphic sole give a geothermal gradient greater than 40 ºC/km, consistent with subduction inception occurring at or near the spreading ridge of the South Loyalty Basin.

3. Outcrop-scale deformation patterns and mineralogy

The study area is exposed at low tide on the foreshore of Plum Beach (south-east of Noumea), across a ~150x100 m surface (Fig. 1b). This area is bounded to the west by the New Caledonia Basin and by a densely vegetated cliff to the east. It is located near the base of the ophiolite, 50 to 100 m above the north-east dipping contact with the underlying Poya unit, which outcrops 2 km to the north.

The study area is a major deformation zone characterized by large-scale mafic shear bands (up to 100 m long in places) and centimetric to decimetric orthopyroxenite veins away from the deformed area. The shear bands and veins cross-cut the peridotite, which is constituted mainly of highly serpentinized harzburgite and rare dunite. One to two meters away from the shear bands, the peridotite is massive and has only a tectonite porphyroclastic texture with a high temperature foliation steeply dipping to the NE (parallel to the paleo-Moho according to Prinzhofer et al., 1980). The orientation of this foliation is discordant with respect to the deformation observed in the mafic shear bands.

Ten major shear bands have been recognized in the study area. Shear bands #1 to #7 are 30 to 50 m long and strike ~N150 (Fig. 1b). They disappear under the eastern cliff but likely extend further to the south-east, where similar shear bands are found in apparent continuity along the coast (#8 to #10). The overall length of these shear bands is thus greater than 150 m.

The shear bands are m- to several m-thick and commonly outlined by 10–50 cm thick amphibolite bands, mostly found at the core of the shear bands (and, when found on the margins, only on their south-west side; Fig. 2).

Peridotite and amphibolite are strongly boudinaged within the amphibolite-bearing shear zones (Fig. 3a,b,c). Strain increases towards the core of the shear bands, as shown by the marked decrease in boudin size, from the m- to the cm- scale. Both ultramafic and mafic boudins are sigmoidal and indicate consistent sinistral-reverse, top to the north-west shear senses across the whole outcrop (Fig. 2,3a). These boudins are embedded in a phlogopite-rich matrix described below.

A network of distributed leucocratic feldspar-rich veins also cross-cuts the peridotite. This network is mainly found on the margins of the high strain bands. Mutual cross-cutting relationships between the dark amphibolites and the feldspar-rich veins suggest that they formed coevally. The vein network is developed only on one side of the amphibolite bands (to the NE); the density, thickness and length of the veins decrease away from the amphibolites (Fig. 3c,d,f,g). The mafic shear band #4bis is a dm-thick dark amphibolite without feldspar-rich veins (Fig. 2).

Amphibolite bands (Fig. 3e) chiefly comprise calcic amphibole with 10 to 50 vol.% plagioclase, variably altered to reddish-to-yellowish low-grade oxidized aggregates. Pyroxene (always orthopyroxene, as detailed below) amounts to 15–30 vol.%.

Leucocratic feldspar-rich veins are characterized by a predominance of plagioclase with up to 20 vol.% coarse-grained orthopyroxene crystals (Fig. 4a,b). Most orthopyroxenes are rimmed by calcic-amphibole.

A light colored, green to grey matrix comprising phlogopite, chlorite, talc and serpentine is observed within the shear bands and appears to form at the expense of both the mafic and ultramafic rocks (Fig. 3c,d,e,f). Late, milky white cm-thick serpentine veinlets rim peridotite boudins and also cross-cut the boudins and the

matrix. Phlogopite is also observed concentrated in m-scale veins next to some of the shear bands (#9).

4. Sampling strategy and analytical techniques

4.1 Sample selection

60 samples (Table 1) were collected in the field across the whole range of textures and mineralogical assemblages of the shear bands (both for mafic -M- and ultramafic -UM- protoliths; Fig. 2). 15 samples are dark amphibolites, either within deformation bands (e.g. M4d; Fig. 2,5a) or isolated in undeformed peridotite (e.g. M8a), whereas 5 samples are deformed feldspar-rich mafic veins (e.g. M8e; Fig. 5b), including an undeformed feldspar-rich veinlet isolated in peridotite (sample M9). Ultramafic samples comprise 17 peridotite boudin samples surrounded by deformed feldspar-rich veins and phlogopite-rich matrix (e.g. UM13, UM10; Fig. 5c,d), 14 undeformed peridotite samples (e.g. UM12, UM14) and one orthopyroxenite vein sample.

4.2 Electron probe microanalysis (*EPMA)*

EPMA was carried out at CAMPARIS (UPMC–IPGP, Paris, France) on amphibolites (n=7), feldspar-rich veins (n=5), peridotite boudins (n=5), undeformed peridotites (n=2) and on the biotite-rich matrix (n=7), using classical analytical conditions for spot analyses (1-2 μm spot size; 15kV, 10nA, wavelength-dispersive spectroscopy mode), using Fe_2O_3 (Fe), $MnTiO_3$ (Mn, Ti), diopside (Mg, Si), CaF_2 (F),

orthoclase (Al, K), anorthite (Ca) and albite (Na) as standards for bracketed elements. Representative analyses are given in Table 2.

4.3 Thermobarometry

Pressure and temperature conditions of crystallization have been estimated using the hornblende-plagioclase geothermobarometer of Holland and Blundy (1994) modified by Anderson and Smith (1995) in three olivine-bearing amphibolites and in six olivine-free amphibolites. This geothermobarometer is based on the reaction: edenite + albite = richterite + anorthite. The absence of Ti-rich phases in amphibolites invalidates the use of Ti-based geothermobarometers. Representative pressure–temperature estimates are given in Table 2.

The Fe^{3+} estimation method in amphibole given in Holland and Blundy (1994) provides the minimum (Fe^{3+}/Fe_{tot}) ratio for which sufficient Na is allocated to the A-site. Fe^{3+}/Fe_{tot} here averages around 0.4 in late amphibole (i.e. magnesio-hornblende). With a (Fe^{3+}/Fe_{tot}) ratio = 1, estimated after the method of Leake et al. (1997), the estimated temperature is ~ 70 ˚C higher than that calculated with Fe^{3+}/Fe_{tot} = 0.4.

4.4 ICPMS and LA-ICPMS:

Whole-rock major element analysis was performed on 7 samples (Table 3) at EOST in Strasbourg, France, by ICP-AES and ICP-MS (see Table 2; analytical procedure given in Omrani et al., 2008) and at UPMC Univ. Paris 6 (following the procedure of Salaün et al. 2010).

LA-ICPMS was performed on amphibole in at IRD Bondy using a 7500 cx AGILENT NI Standards coupled with a laser NWR-213 nm. Analyses were carried

out using a 10 Hz laser repetition rate and 50 µm beam diameter for amphibole. All analyses were conducted at fixed beam position. For internal standardization ^{43}Ca was used for amphibole. For external standardization, NIST SRM 610 and 612 glasses were used after Pearce et al. (1997). Raw data were processed using GLITTER (GEMOC, Macquarie University, Australia). The following masses were analyzed (Table 4): ^{7}Li, ^{11}B, ^{47}Ti, ^{85}Rb, ^{88}Sr, ^{89}Y, ^{90}Zr, ^{93}Nb, ^{133}Cs, ^{138}Ba, ^{139}La, ^{140}Ce, ^{141}Pr, ^{146}Nd, ^{147}Sm, ^{153}Eu, ^{157}Gd, ^{159}Tb, ^{169}Dy, ^{165}Ho, ^{166}Er, ^{172}Yb, ^{175}Lu, ^{178}Hf, ^{181}Ta, ^{208}Pb, ^{238}U, ^{232}Th.

4.5 Radiometric dating

The selected samples were crushed and sieved; single grains of amphibole were handpicked under binocular microscope and cleaned in ultrasonic bath with acetone and distilled water. They were packaged in Al foils and irradiated for 40 hours in the core of the Triga Mark II nuclear reactor of Pavia (Italia) with several aliquots of the Fish Canyon sanidine standard (28.03 ± 0.08 Ma; Jourdan and Renne, 2007) as flux monitor. Argon isotopic interferences on K and Ca were determined by irradiation of KF and CaF_2, pure salts from which the following correction factors were obtained: $(^{40}Ar/^{39}Ar)_K$ = 0.00969 ± 0.00038, $(^{38}Ar/^{39}Ar)_K$ = 0.01297 ± 0.00045, $(^{39}Ar/^{37}Ar)_{Ca}$ = 0.0007474 ± 0.000021 and $(^{36}Ar/^{37}Ar)_{Ca}$ = 0.000288 ± 0.000016. Argon analyses were performed at Géosciences Montpellier (France) with two analytical devices that each consist of: (a) an IR-CO2 laser of 100 kHz used at 5-15% during 60 sec, (b) a lenses system for beam focusing, (c) a steel chamber, kept at 10^{-8} - 10^{-9} bar, with a drilled copper plate, (d) an inlet line for purification of gases including two Zr-Al getters, (e) a multi-collector mass spectrometer (Argus VI from Thermo-Fisher) or an

MAP215-50 single collector mass spectrometer depending on the used device. A custom-made software controls the laser intensity, the timing of extraction/purification and the data acquisition. To measure the Ar background within the system, one blank analysis was performed every three sample analyses. ArArCalc© v2.5.2 was used for data reduction and plotting. The one-sigma errors reported on plateau, isochron and total gas ages include the error on the irradiation factor J. Atmospheric ^{40}Ar was estimated using a value of the initial $^{40}Ar/^{36}Ar$ of 295.5. Data are portrayed as age spectra on figure 11 and summarized in Table 5.

5. Petrography

5.1. Mafic rocks

Dark mafic bands (Fig. 6a,b,c) contain abundant amphibole (40–70 vol.%), plagioclase (10–50 vol.%), orthopyroxene (10–20 vol.%) ± olivine (0–25 vol.%). Olivine is only found in some mafic layers (i.e. shear band #4bis; M8a, Fig. 6c). No clinopyroxene is found. Sulphide inclusions in amphibole, iron oxides and rare apatite (samples M8a and M8b) are also present.

Amphibole surrounds all other mineral phases and appears texturally as a late crystallization product with respect to olivine, orthopyroxene (Fig. 6d,e,g, 7a,b,c,d). Sample M8a show two distinct amphibole-bearing layers as an olivine-free amphibolite vein cross-cut a boudinaged olivine-bearing amphibolite band (Fig 6c). In olivine-bearing amphibolites (shear band #4bis), amphibole (referred to as early amphibole) is strongly pleochroic from blue to green under the microscope with a sub-automorph habitus and marked cleavages (Fig. 6d,g). By contrast, amphibole in

olivine-free amphibolite (referred to as late amphibole) shows a distinctly paler pleochroism and presents a higher degree of deformation (Fig. 6e).

Textural relationships between plagioclase, orthopyroxene and olivine are obscured by the amphibolitization stage. Olivine appears as fine-grained clusters closely associated with, and generally included in, orthopyroxene (Fig. 6g, 7a,b). In sample M4e, olivine was replaced by orthopyroxene before the crystallization of large amphibole grains (Fig. 7c,d). Olivine is also partially destabilized by tremolite. Primary Cr-rich spinel crystals are present in olivine (Fig. 7a). In olivine-bearing samples, plagioclase is rare and partially to totally replaced by amphibole (Fig. 6g).

Leucocratic feldspar-rich veins are mainly composed of plagioclase (70–100%) with subordinate orthopyroxene (0–20%) and rare amphibole (0–10%). Undeformed leucocratic veins show euhedral amphibole in a groundmass of large plagioclase crystals (Fig. 6f). Close to the shear bands, veins of plagioclase evidence deformation and grain size reduction. Orthopyroxene is only partially preserved yet retaining textural evidence of former equilibrium with plagioclase. Orthopyroxene is included in amphibole or rimmed by amphibole pressure shadows (Fig. 6e), again suggesting the partial destabilization of coarse grained primary assemblage of orthopyroxene (± olivine) and plagioclase to form various generations of amphibole. A network of late serpentine, chlorite and talc is observed in orthopyroxene fractures (Fig. 6d).

As for ultramafic rocks, mafic bands are locally replaced by a phlogopite-rich matrix (in which phlogopite is in turn replaced by chlorite). Orthopyroxene and calcic-amphibole appear only as relicts into layers of phlogopite and acicular ortho-amphibole. Plagioclase is destabilized and rimmed by a Ba-rich K-feldspar.

5.2. Ultramafic rocks (UM) and matrix

The mineralogy of undeformed peridotites is dominated by an isotropic network of serpentine (75-90%), with rare relicts of brown orthopyroxene, olivine phenocrysts and black chromiferous spinels. These peridotites belong to the highly depleted harzburgites of the Massif du Sud (i.e. Prinzhofer and Allègre, 1985; Ulrich et al., 2010; Pirard et al., 2013). Few deformation textures are observed, where the extensive late serpentinization may have erased former deformation textures.

Peridotites boudinaged in shear bands (Fig. 7b) show a similar mineral assemblage. However, a reaction rim around peridotite boudins contains coarse-grained hornblende pseudomorphing orthopyroxene, and containing chromite inclusions (Fig. 7g). Light colored phlogopite (Fig. 7b,f,h) and acicular ferro-magnesian ortho-amphibole (Fig. 5f) co-crystallized around peridotite boudins as a result of the partial destabilization of ultramafic orthopyroxene and secondary hornblende. Therefore, this assemblage postdates the boudinage of the peridotite and the first hydration recorded by the crystallization of hornblende. Phlogopite increases in modal proportion towards the amphibole-rich mafic bands, along with a grain size decrease but shows no preferred orientation. Chlorite is interlayered with phlogopite and crystallizes as a late stage alteration product responsible for the macroscopically greenish to greyish color of the matrix. Millimetric veinlets of talc–chlorite–serpentine, slightly sheared in places, also cross-cut peridotites boudins (Fig. 7h). These veinlets are themselves cross-cut by a late isotropic serpentine network.

6. Mineralogy

Orthopyroxene

Orthopyroxene from harzburgites displays a typical Mg# [Mg/(Mg+Fe)] of 0.92 ± 0.02 (Fig. 8a). In mafic rocks, the Mg# of orthopyroxene shows lower values ranging between 0.77 and 0.85.

Cr_2O_3 and CaO contents (Fig. 7a) show small yet systematic variations between the mafic bodies, with higher values in olivine-bearing rocks (< 0.20 wt% Cr_2O_3; 0.35–0.65 wt% CaO, except for three points with 0.82 and 0.97 wt% CaO) than in leucocratic feldspar-rich rocks (< 0.04 wt% Cr_2O_3; 0.15–0.35 wt% CaO). Cr_2O_3 and CaO contents are higher in ultramafic rocks, with large intra-sample variations (0.40-0.80 wt% Cr_2O_3; 0.40-1.80 wt% CaO). Al contents are low (~0.02 p.f.u.) and show no systematic variation.

Orthopyroxene in harzburgite falls within the composition domain of orthopyroxene-poor harzburgite described by Prinzhofer et al. (1980) and Pirard et al. (2013; Fig. 8a). Orthopyroxene in olivine-bearing and olivine free amphibolites overlaps the range of orthopyroxene in amphibolite and hornblendite dikes described by Pirard (2012). Orthopyroxene in mafic bands have similar Mg# orthopyroxene from gabbronorite sills of Pirard et al. (2013), but show lower Ca content.

Olivine

The patterns of Mg# of olivine (Fig. 8b) in harzburgite and in olivine-bearing mafic rocks mirror those of orthopyroxene described above (Fig. 8b). Mg# in ultramafic olivine is 0.91–0.92 and the MnO content varies between 0.06 and 0.22 wt% (Fig. 8b), in the same range as those of nearby harzbugites (Pirard et al., 2013). Olivine in mafic bands shows similar Mg# (0.78-0.85 wt%) to amphibolite and hornblendite dikes of Pirard (2012). The Mg# is lower and the MnO content (0.20–

405 0.39 wt%) is higher than reported for mafic cumulates by Pirard et al. (2013; Fig. 8b).
406 NiO content in mafic olivine varies between 0.16 and 0.21 wt%, which is consistent
407 with the most evolved olivine found in olivine-bearing cumulates (Pirard et al., 2013).
408 Compositional trends in NiO and MnO vs. Mg# match the fractional crystallization
409 trends evidenced by Pirard et al. (2013).

410

411 *Feldspar*

412 Plagioclase occurs only in mafic rocks, as veins in leucocratic feldspar-rich
413 rocks (with a composition of a norite), or as scarce, isolated crystals in olivine-bearing
414 rocks. In noritic rocks, albite content [Na# = Na/(Na+Ca)] ranges from 0.46 to 0.66
415 (from labradorite to andesine; Fig. 8c), in the domain of amphibolite dikes described
416 by Pirard (2012). In olivine-bearing rocks, plagioclase corresponds to anorthite (Na#:
417 0.02–0.07; Fig. 8c), in the range of amphibolite dikes of Pirard (2012). Secondary
418 feldspar rimming norite veins are rich in alkalis (~5.5 wt% Na_2O; ~3.5 wt % K_2O;
419 ~12.5 wt% BaO) and have intermediate composition between anorthoclase and
420 hyalophane.

421

422 *Ca-amphibole*

423 Amphibole shows Mg# comparable to that of orthopyroxene and olivine in both
424 mafic (0.90–0.74; Fig. 9a) and ultramafic rocks (~0.91 ± 0.01; Fig. 9a), and Na < 0.5
425 p.f.u. and $(Ca+Na)_B$ > 1.0 p.f.u. typical of calcic-amphibole (Leake et al., 1997).

426 In olivine-bearing mafic bodies, early amphibole is pargasitic with $(Na+K)_A \geq$
427 0.5 p.f.u and Si ranging from 6.12 to 6.30 p.f.u. (Fig. 9b). Late amphibole
428 destabilizing this pargasite hornblende has $(Na+K)_A \leq 0.5$ p.f.u. and a higher Si

content (6.50–7.00 p.f.u.; Fig. 9b), and belongs to the magnesio-tschermakite hornblende (Leake et al., 1997). In olivine-free samples (i.e M3c), late amphibole shows a decrease in $(Na+K)_A$ and an increase of the Si content (6.37–6.88 p.f.u.; Fig. 9b). This evolution is also observed with the content in Ti (0.15–0.05 p.f.u.). This composition is similar to the composition of amphibole from undeformed mafic dikes described by Pirard (2012), and partially fall in the domain of the metamorphic sole amphibolites from Thio considering their Ti and $(Na+K)_A$ contents, yet with a much lower Mg# (see Cluzel et al., 2012).

Early amphibole in olivine-bearing amphibolite has the lowest Ti (0.01 and 0.05 p.f.u) and does not fall in the domains of amphibole-bearing dikes (Pirard, 2012) or of the metamorphic sole (Cluzel et al., 2012) (Fig. 9c). Amphibole with the highest Si content is again the poorest in $(Na+K)_A$ content (Fig. 9b). Tremolite is only present in olivine-bearing rocks and texturally associated to mafic olivine (Fig. 9b).

Calcic-amphibole destabilizing ultramafic orthopyroxene are magnesio-hornblende with high Si content (7.19–7.46 p.f.u.), $(Na+K)_A$ between 0.25 to 0.12 p.f.u. (Fig. 9b) and Ti < 0.10 p.f.u. (Fig. 9c).

Late acicular amphibole crystallizing within the phlogopite-rich matrix belongs to the ferro-magnesian anthophyllite series (Si ~8 p.f.u; $Al_{tot} \leq 0.23$ p.f.u.; $(Ca+Na)_B \leq 0.15$ p.f.u.; Leake et al., 1997).

Phlogopite

Phlogopite presents a Mg# of 0.89, regardless of its structural position in the shear band (Table 1). Only few crystals display the K_2O content of a regular mica

owing to retrogression by chlorite. Cr_2O_3 (< 0.02 wt%) and TiO_2 (0.05 wt%) are present in small amounts.

Accessory minerals

Early amphibole grains (i.e. pargasite) host various inclusions (e.g. spinel, magnetite, sulfides). Magnetite inclusions derive from the oxidation of iron-sulphide and spinel. Spinel in harzburgite is a chromite with a Cr# [Cr# = (Cr/(Cr+Al+Fe^{3+})] of 0.72 ± 0.05 and a Mg# of 0.35 ± 0.05 (Fig. 9d). Spinel is consistently more aluminous in mafic rocks, with a Cr# from 0.18 to 0.38 for a Mg# varying between 0.25 and 0.32 (Fig. 9d). TiO_2 in mafic and ultramafic spinel is below the detection limit. Cu- and Ni-rich Fe-sulphides (i.e. pentlandite-pyrrhotite) are found as inclusions in early amphibole in olivine-bearing mafic rocks.

7. Geochemistry

7a. Whole rock geochemistry

Rare earth elements (REE) normalized to N-MORB of both olivine-bearing and olivine-free amphibolites display values lower than 1 [$(REE)_N$ ~ 0.4], with the exception of the sample M4f [$(REE)_N$ ~ 1)] (Fig. 10a). They display a slight enrichment in light REE (LREE) relative to heavy REE (HREE) [$(La/Lu)_N$ = 1.89 ± 0.35]. High field strength elements (HFSE; Ti, Hf, Zr, Nb, Ta) are slightly depleted relative to REE [$(Nb/Lu)_N$ = 0.41 ± 0.05] (Fig. 10a). Large Ion Lithophile Elements (LILE; Pb, U, Th, Ba, Rb, Cs) show large enrichments relative to REE, increasing with their degree of mobility and incompatibility [$(Cs/Lu)_N$ = 62 ± 39] (Fig. 10a).

475 The compositions range of metamorphic sole (Cluzel et al., 2012) display a
476 similar pattern to amphibolites though slightly shifted towards higher values by a
477 factor of ~2 (Fig. 10a). Gabbronorite sills (Pirard et al., 2013) are highly depleted in
478 all incompatible elements. However, they display a pattern roughly similar to that of
479 amphibolites, with a mean relative depletion factor of ~10 but with larger Pb and Sr
480 relative anomalies (Fig. 10a). Arc tholeiitic dikes (Cluzel et al., 2006) have
481 incompatible elements compositions overlapping with those amphibolites (Fig. 10a).
482 It strongly suggests that tholeiitic dikes and amphibolites have a same origin.

483 In phlogopite-rich rocks, concentrations in HREE are similar to those of olivine-
484 free and olivine-bearing amphibolite (Fig. 10a). However, phlogopite-rich rocks have
485 a larger enrichment in LREE relative to HREE [$(La/Lu)_N = 3.55 \pm 1.77$]. These rocks
486 are depleted in HFSE relative to REE but less depleted than olivine-bearing and
487 olivine-free amphibolite (with the exception of the sample M4f). Sr shows a large
488 depletion relative to REE and LILE display a large enrichment especially in Cs.

489

490 **7b. In-situ trace elements**

491 Incompatible trace elements compositions of early and late amphibole,
492 respectively found in olivine-bearing and olivine-free amphibolites display similar N-
493 MORB normalized patterns (Fig. 10b) with however slightly higher content in late
494 amphibole (i.e. magnesio-hornblende) compared to early amphibole (i.e. pargasite).
495 REE patterns from heavy REE (HREE) to light REE (LREE) are flat and close to N-
496 MORB values, with $(La/Lu)_N = 0.87 \pm 0.39$. HFSE are slightly depleted relative to
497 REE [$(Nb/Lu)_N = 0.21 \pm 0.07$]. LILE show positive anomalies [$(Cs/Lu)_N = 12.1 \pm$
498 5.9]. Overall, similar behaviors (i.e. negative anomalies in HFSE and positive

anomalies in LILE) are observed in whole-rock data on amphibolites and in-situ data on amphibole, suggesting that the trace element budget in the rocks is mainly controlled by amphibole. However, higher HREE content in late amphibole compared to that in early amphibole is difficult to explain with a fluid mediated recrystallization. This higher content more likely mirrors the more differentiated nature of the norite dikes compared to the troctolite dikes (prior to metamorphic hydration).

Amphibole in mafic amphibole-bearing dikes analyzed by Pirard (2012) displays a pattern similar to that of the amphibole reported here (grey overlay; Fig. 10b): it shows a similar enrichment in Pb and depletions in Ti–Sr–Nb–Ta with comparable absolute values, including in the most mobile and incompatible trace elements, advocating for similar origins. Ba-content is similar in both analyses series and Rb-content is lower in the amphibole of Pirard (2012) than all our early and late amphiboles (Fig. 10b). Cs has not been measured.

8. $^{40}Ar/^{39}Ar$ constraints on mafic rocks formation

$^{40}Ar/^{39}Ar$ laser probe step-heating dating was carried out on 20 isolated single amphibole crystals from 11 different rocks, using the procedure described above. These samples are mainly olivine-free and olivine-bearing amphibolites from the Plum beach. They also include amphibolites from the Thio metamorphic sole (sample C10) and undeformed gabbroic dikes from the Massif du Sud (samples SNC03 and SNC04, col des Deux Tétons). Age spectra and inverse isochron plots are reported on figure 11 for some of these samples. The closure temperature for the $^{40}Ar/^{39}Ar$ method in hornblende is around 550 ± 50 ºC (Harrison, 1981). For most samples,

errors are relatively large due to the fact that only one grain was analyzed each time and that the K content (and therefore the amount of radiogenic Ar) is low in these amphiboles.

Amphibole from the Thio metamorphic sole provides an age of 56.9 ± 2.6 Ma (Fig. 11a,12) consistent with the age reported by Cluzel et al. (2012) from a nearby exposure. Similar ages are obtained on the two undeformed gabbros from the Massif du Sud for which intercept ages are in the range 51–52 ± 4 Ma (Fig. 11a,12; see the Online Fig. S1 for isotope correlation plot), with initial $^{40}Ar/^{36}Ar$ values close to the present-day atmospheric ratio (see Table 5). Large amphibole from a partially weathered pegmatite dike yields more scattered results with some evidence of excess argon as a result of fluid infiltration and only a maximum age of 60 ± 5 Ma can be attributed to this sample.

At Plum beach, 8 hornblende crystals from 4 olivine-free amphibolites (M3d, M4d, M8a-Z2, M8f) and 5 hornblende crystals from two weakly deformed olivine-bearing amphibolite (M15 and M8a-Z1) yield ages ranging between 54 and 93 Ma, with the exception of one crystal (M15) that displays a strongly discordant age pattern and an integrated age of 167 ± 21 Ma likely related to trapped excess argon. For M8f, 4 amphiboles were analyzed and representative age spectra are shown on figure 11b, with plateau dates ranging from 54.9 ± 2.0 Ma to 59.2 ± 2.7 Ma and a similar age in the isotope correlation plot with an initial atmospheric ratio (reported in the Online Fig. S1). The consistency of the results on 4 grains from M8f and the lack of evidence of excess argon for this sample suggest that amphibolitisation and related deformation occurred at ca. 55 Ma, which is supported by the age of 54.1 ± 3.4 Ma obtained on amphibolite M3b from another shear zone. According to microprobe analyses and textural observations, it is likely that this age of ca. 55 Ma corresponds to the

548 crystallization of secondary magnesio-hornblende that partially replaced pargasite and
549 orthopyroxene. This age range coincides with the formation of the metamorphic sole
550 at Thio (sample C10 and Cluzel et al., 2012), the emplacement of some gabbros
551 (samples SNC03 and SNC04) and pre-obduction felsic dikes (53 Ma; Cluzel et al.,
552 2006).

553 8 amphiboles from 5 olivine-bearing samples yield older ages ranging from 73
554 to 93 Ma (Table 5) with relatively discordant age spectra (Fig. 11c) and large
555 experimental errors due to the low amount of K. However, the isotope correlation
556 diagram and the flat K/Ca ratios do not provide evidence of excess argon (reported in
557 the Online Fig. S1), which could indicate that ages around 90 Ma are meaningful.
558 This suggests that early amphibole is preserved in the dated rocks, which is consistent
559 with the chemical data that point to the coexistence of primary pargasite predating
560 synkinematic magnesio-hornblende developed around it.

561 # 9. Interpretations and discussion

562 ## 9.1. Nature of the protolith and subduction signature

563 The sharp contact between mafic rocks and surrounding peridotites (preserved
564 from metasomatic alteration in places) suggests that these mafic rocks were emplaced,
565 prior to amphibolitization, as 100 m-scale intrusions, most likely as dikes or melt
566 lenses. The lack of pervasive deformation in the peridotite a few meters away from
567 the shear bands, and the presence of olivine and orthopyroxene in mafic rocks, rule
568 out the possibility that the mafic bands represent sheared metamorphic sole
569 amphibolites imbricated within mantle wedge peridotites. The protolith of the mafic
570 bands is therefore interpreted as emplaced in the form of small-scale melt intrusions at
571 temperatures where peridotites were comparatively brittle.

572 Partially preserved orthopyroxene, anorthitic plagioclase and high Mg# olivine
573 indicate that the protolith of the amphibolite bands was a norite or a troctolitic norite.
574 Late hornblende (i.e. magnesio-hornblende) and Ca–Na plagioclase, which abound in
575 amphibolite bands, may have recrystallized from orthopyroxene, olivine and
576 anorthitic plagioclase (such as found in the "noritic" pods) during amphibolitisation
577 and/or later fluid infiltration. Clinopyroxene was either absent or is now completely
578 replaced (undeformed hornblendite dikes from Rivière des Pirogues show late
579 amphibole replacing large clinopyroxene crystals; Pirard, 2012).

580 Olivine-bearing domains cross-cut by olivine-free domains (Fig. 6c) point to
581 evolving compositions of the magma intruding the peridotite. The positive correlation
582 between Cr# of spinel and Mg# of olivine in olivine-bearing amphibolites suggests
583 that the mafic protolith formed through melting of harzburgite with a supra-
584 subduction signature followed by fractional crystallization (Marchesi et al., 2009).
585 The presence of orthopyroxene, plagioclase and early amphibole (i.e. pargasite) is
586 consistent with peridotite melting triggered by aqueous slab-derived fluids (Pirard,
587 2012).

588 Amphibolites display flat N-MORB normalized patterns with lower REE
589 abundances than N-MORB ($REE_{Amphibolite}$ / $REE_{N\text{-}MORB}$ ~0.5; Fig. 10). A simple
590 melting model shows that these amphibolites are too enriched, however, to derive
591 directly from melting of the host depleted harzburgite and require a less depleted
592 ultramafic source (either refertilized by fluids or silica-rich melts). Trace elements
593 patterns of amphibolites in fact closely fit those of unmetamorphosed microdioritic
594 dikes found in the Massif du Sud, interpreted as subduction-related magma intrusions
595 by Cluzel et al. (2006).

The slab signature is best recorded by HFSE and LILE. HFSE in the bulk rock display negative anomalies relative to REE (Fig. 10). These are characteristic of subduction zone magmas, as these elements are retained in rutile and zircon in the subducting slab (e.g. Coltorti et al., 2007; Zack and John, 2007). The enrichment in LILE (and to a lesser extent in LREE) is also consistent with a subduction signature, since LILE are mobilized during the dehydration of the upper part of the slab (e.g. Pearce et al. 1984). Such enrichments are observed in metamorphic soles for Rb, Ba and also Pb (Ishikawa et al., 2005). These enrichments cannot result from late sub-surface alteration, since LILE and HFSE are mainly concentrated in high temperature amphiboles which impose their geochemical signature in the whole rock (Fig. 10b; Table 4).

9.2 Petrological evolution, deformation and fluid ingression

Field relationships and mineralogy suggest that the dark amphibolite bands and the more leucrocratic noritic veins are cogenetic, with percolation apparently favored towards the north. This direction is compatible with upward melt migration expected at plate boundary (e.g. Matthews et al., 2015) within the mantle wedge (Fig. 2, 13a) and close to the nascent crust (e.g. Pirard et al., 2013). Progressive aqueous fluid infiltration and amphibolitization of the preexisting mafic bands would have preferentially localized deformation in the former dikes during the first stages of the Eocene subduction. Fig. 4c and Fig. 5c exemplify mafic veins with peridotite boudins. Deformation localization is here closely tied with fluid infiltration, consistently with the weaker rheology of amphibole and plagioclase compared to pyroxene (Homburg et al., 2010) and olivine.

Three main hydration stages can be seen in these rocks and related to deformation events, as schematized in Fig. 13:

— *(a) amphibolitization stage:*

Replacement of orthopyroxene by late amphibole is the second event of hydrous fluid intrusion and the major deformation stage (Fig. 13b). Whereas magnesio-hornblende in undeformed leucocratic veins has an euhedral shape and are associated to a groundmass of large plagioclase crystals (Fig. 6f), magnesio-hornblende within the shear bands makes up the foliation, together with plagioclase (Fig. 6e), and presents syn-kinematic texture (e.g. pressure shadow around orthopyroxene; Fig. 6e). Euhedral late amphibole could be of magmatic origin, but syn-kinematically deformed late amphibole has likely crystallized from an aqueous fluid. Nonetheless, evolving late amphibole (and possibly plagioclase) compositions (Fig. 8c, 9b,c) indicate that mafic bands underwent progressive recrystallization during fluid infiltration and deformation (localized within the shear bands).

Although mafic bands are strongly boudinaged and folded, amphibole crystals themselves are only mildly deformed. This is consistent with plagioclase being weaker than amphibole (Getsinger and Hirth, 2014) and with some static recrystallization after the peak of deformation. Peridotites in contact with mafic dikes are also boudinaged during this stage and record hydration through the crystallization of amphibole with a Mg# around 0.92 (Fig. 9a).

Magnesio-hornblende (i.e. late amphibole) compositions yield pressure-temperature conditions 3–5 kbar and 750 ± 50 ºC (Table 2). These estimations are similar to that calculated for leucodiorite dikes in the uppermost harzburgite (i.e. 3.5 ±

643 0.6 kbar and 800 ± 45 ˚C; Pirard, 2012). As for metamorphic sole, the pressure
644 estimates for the dikes cannot be explained by the present ophiolite thickness.

645 Age constraints on amphibole reveal an age cluster at 55 ± 2 Ma (Fig. 12),
646 which is well defined for late amphibole. Although the closure temperature for the
647 $^{40}Ar/^{39}Ar$ method in hornblende is ~200 ºC lower than our temperature estimates for
648 amphibole formation, we interpret these ages as crystallization ages in a context of
649 fast cooling. Considering available constraints on the latest oceanic magmatic events,
650 pressure–temperature estimates and the age of the New Caledonia metamorphic sole
651 (Cluzel et al., 2012 and this study), high temperature metamorphism and cooling
652 below the closure temperature must have occurred in a very short lapse of time after
653 the Eocene subduction initiation.

654 — *(b) formation of the alkali-rich matrix:*

655 The alkali-rich matrix is composed of an association of Ba-rich feldspar,
656 phlogopite and ortho-amphibole crystallized at the expense of pyroxene, olivine and
657 Ca-amphibole, from both the mafic and ultramafic protoliths, with less deformation
658 than during the main amphibolitization stage (Fig. 13c). This matrix points to an
659 episode of fluid ingression postdating amphibolitization, with a markedly distinct
660 fluid composition (i.e. richer in K, Na and Ba). Ortho-amphibole (anthophyllite)
661 indicates temperatures of ~700 ± 50 °C (Chernosky and Autio, 1979, Nozaka, 2011).

662 — *(c) Late reaction with serpentine, talc, chlorite:*

663 Finally, veinlets composed of hydrous phases (serpentine, talc and chlorite)
664 form mm to cm-scale rims around mafic and peridotite boudins or cross-cut the
665 matrix (Fig. 13d). With temperatures lower than 500–600 °C, according to presence

of the talc–chlorite assemblage, this stage reflects the latest and coldest episode of reequilibration of these shear bands.

9.3. Geodynamics implications

Both petrology and geochemistry (through the similarity to undeformed amphibole-bearing dikes reported in the Massif du Sud; Cluzel et al., 2006; Pirard, 2012) suggest that mafic shear bands correspond to former hm- to km-scale mafic intrusions emplaced in the highly refractory host harzburgite, deriving from the melting of a moderately depleted mantle source fluxed by subduction-derived fluids (see § 9.1).

Trace element geochemistry (i.e. HFSE depletion and LILE enrichment) and age constraints at ca. 55 Ma (Fig. 12) show that secondary amphibolitization coincides with the east-dipping subduction initiation preluding to obduction (Spandler et al., 1995; Cluzel et al., 2001, 2012). Fluid infiltration and at least part of the trace element enrichment could result from dehydration of the upper part of the slab (as for metamorphic sole dehydration; Ishikawa et al., 2005). In this interpretation, the shear bands reported here are a direct record of early subduction processes in New Caledonia, deformation and mantle metasomatism in an active subduction setting.

By contrast, the magmatic origin of the mafic protoliths remains uncertain. The high degree of amphibolitization affecting these mafic dikes hampers modeling the degree of partial melting of the peridotites and to constrain the exact origin of the mafic protoliths.

Age constraints on amphiboles at both ca. 90 Ma (early pargasite) and ca. 55 Ma (magnesio-hornblende) can be accounted for in two different ways:

690 (1) amphibole-bearing troctolite to norite mafic intrusions would have formed at
691 ca. 55 Ma as a result of the east-dipping subduction preluding to obduction, as for the
692 relatively abundant dikes interpreted as supra-subduction and dated at ca. 55 Ma by
693 Cluzel et al. (2006) or dikes found in the nearby Massif du Sud exposures (also
694 interpreted as Eocene, based on structural data; Pirard, 2012), both interpreted as
695 formed in a supra-subduction setting at the expense of a metasomatized, HFSE-
696 depleted mantle. In this view, ages at ca. 90 Ma would be attributed to excess argon.

697 (2) mafic intrusions would represent inherited mafic melts from the Cretaceous
698 South Loyalty basin accretion (dating back to ≥ 90 Ma; e.g. Cluzel et al., 2012 and
699 this study), as several early amphiboles yield an age of ca. 90 Ma (Fig. 12). This
700 hypothesis is supported by the similarity with ages found in amphibole-bearing dikes
701 in the Massif du Sud by Prinzhofer (1981). Hydrous mafic melt intrusions would have
702 been emplaced possibly as a result of the west-dipping Pacific subduction, and later
703 been fluxed by fluids leading to late amphibole crystallization and ages at ca. 55 Ma
704 (during the second, east-dipping subduction initiation). This secondary high
705 temperature event has only partially reset the ca. 90 Ma age in pargasite.

706 The second interpretation is favored by the lack of evidence for excess argon,
707 early amphibole (pargasite) compositions that are distinct from those of Pirard (2012),
708 and the peculiar deformation of these dikes (those of Pirard and Cluzel are not or only
709 mildly deformed).

710 Deformation and fluid infiltration later localized on these preexisting mafic
711 intrusions. Shear bands developed as a result of a threefold stage of fluid infiltration
712 from slab-derived fluids. These mafic bands (and the later metasomatic matrix) are
713 good witnesses of the subduction initiation processes, both in terms of fluid influx and
714 progressive deformation near the base of the obducted New Caledonia ophiolite, from

715 temperatures of 800–700 °C down to less than 600 °C. Localization of deformation
716 along inherited structures such as mafic dike swarms also supports the view that
717 subduction initiation is generally triggered near a preexisting weakness zone (i.e.
718 Agard et al., 2014).

719

720 ## 10. Conclusions

721 This study focuses on strongly sheared mafic amphibolites within the uppermost
722 mantle of the New Caledonia obducted ophiolite, near the transition zone and ~50–
723 100 m above the basal thrust contact. Using a combination of petrological,
724 geochemical, and geochronological data, we show that these amphibolites record
725 melting and polyphase metasomatism within the mantle wedge during the early
726 history of the subduction.

727 Shear bands indicate that deformation and high temperature fluid infiltration
728 (from ~ 800 to ~500 °C) localized along preexisting hm-scale mafic intrusions
729 emplaced within the upper mantle of the New Caledonia ophiolite and derived from
730 peridotites refertilized by slab-derived fluids in a supra-subduction zone environment.
731 The timing of these melt intrusions remains uncertain. Age constraints on early
732 amphibole at ca. 90 Ma and the lack of evidence for argon excess suggest that they
733 could be inherited from the former west-dipping Pacific subduction.

734 Secondary deformation and amphibolitization of these mafic dikes were the
735 result of a threefold infiltration of slab-derived fluids. The age cluster of amphibole at
736 ca. 55 Ma indicates that amphibolitization of the mafic protoliths (as well as later
737 alkali-metasomatism) relate to the onset of the Eocene east-dipping subduction
738 initiation preluding to the obduction of the New Caledonia ophiolite.

These outcrops bring important information on the processes and timing of fluid influx, progressive deformation and peridotites refertilization during subduction initiation, showing how m- to hm-scale heterogeneities (inherited or early-emplaced magmatic dikes) localize deformation and metasomatism in the oceanic lithosphere. In turn this suggests that similar small-scale heterogeneities may have controlled the development of larger thrusts, ultimately leading to the tectonic slicing (and later emplacement) of the New Caledonia ophiolite.

Acknowledgments

We thank M. Ulrich (IPGS, France) for interesting discussions. We also thank B. Caron and O. Boudouma (ISTeP–UPMC, France), M. Fialin and N. Rividi (CAMPARIS), F. Le Cornec (IRD Bondy, France) and D. Deldicque (ENS Paris, France) for analytical support, M. Moroni (ISTeP–UPMC) for the scanning of thin-sections. C. Pirard and J. Hermann are warmly thanked for their constructive reviews and suggestions, and Marco Scambelluri for his editorial handling. This work was essentially funded through the ONLAP project (ANR blanche, SIMI6; 2010 BLAN 615 01). Additional support was provided by an IUF grant (Institut universitaire de France) to Philippe Agard.

References

Agard, P., Jolivet, L., Vrielynck, B., Burov, E., & Monié, P., 2007. Plate acceleration: The obduction trigger? Earth and Planetary Science Letters 258 (3-4), 428–441. doi:10.1016/j.epsl.2007.04.002

761 Agard, P., Zuo, X., Funiciello, F., Bellahsen, N., Faccenna, C., & Savva, D., 2014. Obduction: Why,
762 how and where. Clues from analog models. Earth and Planetary Science Letters 393, 132–145.
763 doi:10.1016/j.epsl.2014.02.021

764 Aitchison, J. C., Clarke, G. L., Meffre, S., & Cluzel, D., 1995. Eocene arc-continent collision in New
765 Caledonia and implications for regional southwest Pacific tectonic evolution. Geology 23 (2),
766 161–164. doi:10.1130/0091-7613

767 Anderson, J. L., & Smith, D. R., 1995. The effects of temperature and fO_2 on the Al-in-hornblende
768 barometer. American Mineralogist, 80, 549–559.

769 Boschi, C., Früh-Green, G. L., Delacour, A., Karson, J. A., & Kelley, D. S., 2006. Mass transfer and
770 fluid flow during detachment faulting and development of an oceanic core complex, Atlantis
771 Massif (MAR 30°N). Geochemistry, Geophysics, Geosystems 7. doi:10.1029/2005GC001074

772 Boudier, F., Ceuleneer, G., & Nicolas, A., 1988. Shear zones, thrusts and related magmatism in the
773 Oman ophiolite: Initiation of thrusting on an oceanic ridge. Tectonophysics 151 (1-4), 275–296.
774 doi:10.1016/0040-1951(88)90249-1

775 Carson, C., Clarke, G., & Powell, R., 2000. Hydration of eclogite, Pam Peninsula, New Caledonia.
776 Journal of Metamorphic Geology 18, 79–90. doi:10.1046/j.1525-1314.2000.00245.x

777 Ceuleneer, G., Nicolas, A., & Boudier, F., 1988. Mantle flow patterns at an oceanic spreading The
778 Oman peridotites record. Tectonophysics 151, 1–26. doi:10.1016/0040-1951(88)90238-7

779 Chernosky, J. V., & Autio, L. K., 1979. The stability of anthophyllite in the presence of quartz.
780 *American Mineralogist*, *64*, 294–303.

781 Clarke, G. L., Aitchison, J. C., & Cluzel, D., 2006. Eclogites and Blueschists of the Pam Peninsula, NE
782 New Caledonia: a Reappraisal. Journal of Petrology *38* (7), 843–876.
783 doi:10.1093/petroj/38.7.843

784 Cluzel, D., Picard, C., C Aitchison, J., Laporte, C., Meffre, S., & Parat, F., 1997. The Poya Nappe, ex-
785 "Formation des Basaltes" (New Caledonia, southwest Pacific): a Campanian to Upper
786 Palaeocene oceanic plateau obducted in the late Eocene. C. R. Acad. Sci., 324, 443–451.

787 Cluzel, D., Aitchison, J. C., & Picard, C., 2001. Tectonic accretion and underplating of mafic terranes
788 in the Late Eocene intraoceanic fore-arc of New Caledonia (Southwest Pacific): geodynamic
789 implications. Tectonophysics 340 (1–2), 23–59. doi:10.1016/S0040-1951(01)00148-2

790 Cluzel, D., Bosch, D., Paquette, J. L., Lemennicier, Y., Montjoie, P., & Ménot, R. P., 2005. Late
791 Oligocene post-obduction granitoids of New Caledonia: A case for reactivated subduction and
792 slab break-off. Island Arc, 14(3), 254–271. doi:10.1111/j.1440-1738.2005.00470.x

793 Cluzel, D., Meffre, S., Maurizot, P., & Crawford, A. J., 2006. Earliest Eocene (53 Ma) convergence in
794 the Southwest Pacific: evidence from pre-obduction dikes in the ophiolite of New Caledonia.
795 Terra Nova 18 (6), 395–402. doi:10.1111/j.1365-3121.2006.00704.x

796 Cluzel, D., Jourdan, F., Meffre, S., Maurizot, P., & Lesimple, S., 2012. The metamorphic sole of New
797 Caledonia ophiolite: 40Ar/39Ar, U-Pb, and geochemical evidence for subduction inception at a
798 spreading ridge. Tectonics 31 (3), TC3016. doi:10.1029/2011TC003085

799 Coleman, R. G. (1971). Tectonic Eraplacement Upper Mantle Peridotires along Continental Edges.
800 Journal of Geophysical Research 76 (5), 1212–1222. doi:10.1029/JB076i005p01212

801 Collot, J. Y., Malahoff, A., Recy, J., Latham, G., & Missegue, F., 1987. Overthrust emplacement of
802 New Caledonia Ophiolite: Geophysical evidence. Tectonics *6* (3), 215–232.
803 doi:10.1029/TC006i003p00215

804 Coltorti, M., Bonadiman, C., Faccini, B., Grégoire, M., O'Reilly, S. Y., & Powell, W., 2007.
805 Amphiboles from suprasubduction and intraplate lithospheric mantle. Lithos 99 (1-2), 68–84.
806 doi:10.1016/j.lithos.2007.05.009

807 Constantin, M., 1999. Gabbroic intrusions and magmatic metasomatism in harzburgites from the
808 Garrett transform fault: implications for the nature of the mantle–crust transition at fast-spreading

809 ridges. Contributions to Mineralogy and Petrology 136 (1-2), 111–130.
810 doi:10.1007/s004100050527

811 Dewey, J. F., & Bird, J. M., 1971. Origin and Emplacement of the Ophiolite Suite: Appalachian
812 Ophiolites in Newfoundland. Journal of Geophysical Research 76 (14).
813 doi:10.1029/JB076i014p03179

814 Eissen, J., Crawford, A., Cotten, J., & Meffre, S., 1998. Geochemistry and tectonic significance of
815 basalts in the Poya Terrane, New Caledonia. Tectonophysic*s* 284, 203–219. doi:10.1016/S0040-
816 1951(97)00183-2

817 Ernewein, M., Pflumio, C., & Whitechurch, H., 1988. The death of an accretion zone as evidenced the
818 magmatic history of the Sumail ophiolite (Oman). Tectonophysics 151, 247–274.
819 doi:10.1016/0040-1951(88)90248-X

820 Gaggero, L., & Cortosegno, L., 1997. Metamorphic evolution of oceanic gabbros: recrystallization
821 from subsolidus to hydrothermal conditions in the MARK area (ODP Leg 153). Lithos 40 (2–4),
822 105-131. doi:10.1016/S0024-4937(97)00006-6

823 Getsinger, a. J., & Hirth, G., 2014. Amphibole fabric formation during diffusion creep and the rheology
824 of shear zones. Geology 42 (6), 535–538. doi:10.1130/G35327.1

825 Godard, M., Jousselin, D., & Bodinier, J.L., 2000. Relationships between geochemistry and structure
826 beneath a palaeo-spreading centre: a study of the mantle section in the Oman ophiolite. Earth and
827 Planetary Science Letters 180 (1–2), 133–148. doi:10.1016/S0012-821X(00)00149-7

828 Godard, M., Dautria, J.-M., & Perrin, M., 2003. Geochemical variability of the Oman ophiolite lavas:
829 Relationship with spatial distribution and paleomagnetic directions. Geochemistry, Geophysics,
830 Geosystems 4 (6). doi:10.1029/2002GC000452

831 Holland, T., & Blundy, J., 1994. Non-ideal interactions in calcic amphiboles and their bearing on
832 amphibole-plagioclase thermometry. Contributions to Mineralogy and Petrology 116 (4), 433–
833 447. doi:10.1007/BF00310910

834 Homburg, J. M., Hirth, G., & Kelemen, P. B., 2010. Investigation of the strength contrast at the Moho:
835 A case study from the Oman Ophiolite. Geology 38 (8), 679–682. doi:10.1130/G30880.1

836 Honnorez, J., Mevel, C., & Montigny, R., 1984. Occurrence and significance of gneissic amphibolites
837 in the Vema fracture zone, equatorial Mid-Atlantic Ridge. Geological Society, London, Special
838 Publications 13 (1), 121–130. doi:10.1144/GSL.SP.1984.013.01.11

839 Ishikawa, T., Fujisawa, S., Nagaishi, K., & Masuda, T., 2005. Trace element characteristics of the fluid
840 liberated from amphibolite-facies slab: Inference from the metamorphic sole beneath the Oman
841 ophiolite and implication for boninite genesis. Earth and Planetary Science Letters 240 (2), 355–
842 377. doi:10.1016/j.epsl.2005.09.049

843 Jourdan, F., & Renne, P. R., 2007. Age calibration of the Fish Canyon sanidine $^{40}Ar/^{39}Ar$ dating
844 standard using primary K-Ar standards. Geochimica et Cosmochimica Acta 71 (2), 387–402.
845 doi:10.1016/j.gca.2006.09.002

846 Lagabrielle, Y., Chauvet, A., Ulrich, M., & Guillot, S., 2013. Passive obduction and gravity-driven
847 emplacement of large ophiolitic sheets: The New Caledonia ophiolite (SW Pacific) as a case
848 study? Bul. Soc. Géo. Fr., 184 (6), 545–556. doi:10.2113/gssgfbull.184.6.545

849 Le Mée, L., Girardeau, J., & Monnier, C., 2004. Mantle segmentation along the Oman ophiolite fossil
850 mid-ocean ridge. Nature 432 (7014), 167–72. doi:10.1038/nature03075

851 Leake, B. E., Woolley, A. R., Arps, C. E. S., Gilbert, M. C., Grice, J. D., Hawthorne, F. C., Whittaker,
852 E. J. W., 1997. Nomenclature of amphiboles. The Canadian Mineralogist 35, 219–246.

853 Marchesi, C., Garrido, C. J., Godard, M., Belley, F., & Ferré, E., 2009. Migration and accumulation of
854 ultra-depleted subduction-related melts in the Massif du Sud ophiolite (New Caledonia).
855 Chemical Geology 266 (3-4), 171–186. doi:10.1016/j.chemgeo.2009.06.004

856 Matthews, K. J., Williams, S. E., Whittaker, J. M., Müller, R. D., Seton, M., & Clarke, G. L., 2015.
857 Geologic and kinematic constraints on Late Cretaceous to mid Eocene plate boundaries in the
858 southwest Pacific. Earth-Science Reviews, 140, 72–107. doi:10.1016/j.earscirev.2014.10.008

McLeod C. J., Lissenbourg J., & Bibby L. E., 2013. “Moist MORB” axial magmatism in the Oman ophiolite: The Evidence against a mid-ocean ridge origin. Geology 41 (4), 459-462. doi:10.1130/G33904.1

Moores, E. M., Kellogg, L. H., & Dilek, Y., 2000. Tethyan ophiolites, mantle convection, and tectonic “historical contingency”: A resolution of the “ophiolite conundrum.” Geological Society of America Special Paper 349.

Moutte, J., (1979). Le massif de Tiébaghi, Nouvelle Calédonie et ses gîtes de chromite. Ecole Nationale Supérieure des Mines de Paris. p. 160

Nicolas, A., 1989. Principes de Tectonique. Masson (ed.), p. 190.

Nicolas, A., Boudier, F., Ildefonse, B., & Ball, E., 2000. Accretion of Oman and United Arab Emirates ophiolite – Discussion of a new structural map. Marine Geophyiscal Research 21, 147–179. doi:10.1023/A:1026769727917

Nozaka, T., 2011. Constraints on anthophyllite formation in thermally metamorphosed peridotites from southwestern Japan. Journal of Metamorphic Geology 29 (4), 385–398. doi:10.1111/j.1525-1314.2010.00921.x

Omrani, J., Agard, P., Whitechurch, H., Benoit, M., Prouteau, G., & Jolivet, L., 2008. Arc-magmatism and subduction history beneath the Zagros Mountains, Iran: A new report of adakites and geodynamic consequences. Lithos 106 (3–4), 380–398. doi:10.1016/j.lithos.2008.09.008

Paris, J. P., Andreieff, P., & Coudray, J., 1979. Sur l’âge Eocène supérieur de la mise en place de la nappe ophiolitique de Nouvelle-Calédonie. Compt. Rend. Acad. Sci. Paris 288, 1659-1661.

Pearce, J. A., Lippard, S. J., & Roberts, S., 1984. Characteristics and tectonic significance of supra-subduction zone ophiolites. Geological Society, London, Special Publications 16 (1), 77–94. doi:10.1144/GSL.SP.1984.016.01.06

Pearce, N. J. G., Perkins, W. T., Westgate, J. A., Jackson, S. E., Neal, C. R., Chenery, S. P., & Gorton, M. P., 1997. A Compilation of New and Published Major and Trace Element Data for NIST

884 SRM 610 and NIST SRM 612 Glass Reference Materials. The Journal of Geostandards and
885 Geoanalysis, 21 (1), 115–144. doi:10.1111/j.1751-908X.1997.tb00538.x

886 Picazo, S., Cannat, M., Delacour, A., Escartín, J., Rouméjon, S., & Silantyev, S., 2012. Deformation
887 associated with the denudation of mantle-derived rocks at the Mid-Atlantic Ridge 13°-15°N: The
888 role of magmatic injections and hydrothermal alteration. Geochemistry, Geophysics, Geosystems
889 13 (4). doi:10.1029/2012GC004121

890 Pirard, C., 2012. Transfer of melts in the sub-arc mantle: Insights from high-pressure experiments and
891 from the New Caledonia ophiolite. College of Physical and Mathematical Sciences.

892 Pirard, C., Hermann, J., & O'Neill, H. S. C., 2013. Petrology and Geochemistry of the Crust-Mantle
893 Boundary in a Nascent Arc, Massif du Sud Ophiolite, New Caledonia, SW Pacific. Journal of
894 Petrology 54 (9), 1759–1792. doi:10.1093/petrology/egt030

895 Prinzhofer, A., Nicolas, A., Cassard, D., Moutte, J., Leblanc, M., Paris, J.-P., & Rabinovitch, M., 1980.
896 Structures in the new caledonia peridotites-gabbros: implications for oceanic mantle and crust.
897 Tectonophysics, 69, 85–112.

898 Prinzhofer, A., 1981. Structure et pétrologie d'un cortège ophiolitique: le Massif du Sud (Nouvelle
899 Calédonie) : la transition manteau-croûte en milieu océanique. École Nationale Supérieure des
900 Mines de Paris. p. 185

901 Prinzhofer, A., & Allègre, C. J., 1985. Residual peridotites and the mechanisms of partial melting.
902 Earth and Planetary Science Letters 74, 251–265.

903 Salaün, A., Villemant, B., Semet, M. P., Staudacher, T., 2010. Cannibalism of olivine-rich cumulate
904 xenoliths during the 1998 eruption of Piton de la Fournaise (La Réunion hotspot): Implications
905 for the generation of magma diversity. Jour. Volcanol. Geotherm. Res. 198, 187–204
906 doi:10.1016/j.jvolgeores.2010.08.022

907 Schellart, W. P., Lister, G. S., & Toy, V. G., 2006. A Late Cretaceous and Cenozoic reconstruction of
908 the Southwest Pacific region: Tectonics controlled by subduction and slab rollback processes.
909 Earth-Science Reviews, 76 (3–4), 191–233. doi:10.1016/j.earscirev.2006.01.002

910 Shervais, J. W., 2001. Birth, death, and resurrection: The life cycle of suprasubduction zone ophiolites.
911 Geochemistry, Geophysics, Geosystems 2. doi:10.1029/2000GC000080

912 Spandler, C., Rubatto, D., & Hermann, J., 2005. Late Cretaceous-Tertiary tectonics of the southwest
913 Pacific: Insights from U-Pb sensitive, high-resolution ion microprobe (SHRIMP) dating of
914 eclogite facies rocks from New Caledonia. Tectonics 24 (3). doi:10.1029/2004TC001709

915 Stern, R., & Bloomer, S. H., 1992. Subduction zone infancy: Examples from the Eocene Izu-Bonin-
916 Marinana and Jurassic California arcs. Bulletin of the Geological Society of America 104 (12),
917 1621–1636. doi:10.1130/0016-7606

918 Sun, S. S., & McDonough, W. F., 1989. Chemical and isotopic systematics of oceanic basalts:
919 implications for mantle composition and processes. Geological Society, London, Special
920 Publications 42 (1), 313–345. doi:10.1144/GSL.SP.1989.042.01.19

921 Ulrich, M., Picard, C., Guillot, S., Chauvel, C., Cluzel, D., & Meffre, S., 2010. Multiple melting stages
922 and refertilization as indicators for ridge to subduction formation: The New Caledonia ophiolite.
923 Lithos 115 (1–4), 223–236. doi: 10.1016/j.lithos.2009.12.011

924 Van De Beuque, S., Auzende, J., Lafoy, Y., Bernardel, G., Nercessian, A., Regnier, M., Exon, N.,
925 1998. Transect sismique continu entre l'arc des Nouvelles-Hebrides de l'Australie: programme
926 FAIJST (French Australian Seismic Transect) Continuous seismic transect between the New
927 Hebrides Arc and the Eastern. Earth and Planetary Sciences 327, 761–768. doi:10.1016/S1251-
928 8050(99)80048-2

929 Vaughan, A. P. M., & Scarrow, J. H., 2003. Ophiolite obduction pulses as a proxy indicator of
930 superplume events? Earth and Planetary Science Letters 213 (3-4), 407–416. doi:10.1016/S0012-
931 821X(03)00330-3

Vitale Brovarone, A., & Agard, P., 2013. True metamorphic isograds or tectonically sliced metamorphic sequence? New high-spatial resolution petrological data for the New Caledonia case study. Contributions to Mineralogy and Petrology 166 (2), 451–469. doi:10.1007/s00410-013-0885-2

Wakabayashi, J., & Dilek, Y., 2003. What constitutes "emplacement" of an ophiolite?: Mechanisms and relationship to subduction initiation and formation of metamorphic soles. Geological Society, London, Special Publications 218 (1), 427–447. doi:10.1144/GSL.SP.2003.218.01.22

Weissel, J. K., & Hayes, D. E., 1977. Evolution of the Tasman Sea reappraised. Earth and Planetary Science Letters 36, 77–84. doi:10.1016/0012-821X(77)90189-3

Whitney, D. L., & Evans B. W., 2010. Abbreviations for names of rock-forming minerals. American Mineralogist 95, 185-197.

Xiong, Q., Zheng, J. P., Griffin, W. L., O'Reilly, S. Y., & Pearson, N. J., 2014. Pyroxenite Dykes in Orogenic Peridotite from North Qaidam (NE Tibet, China) Track Metasomatism and Segregation in the Mantle Wedge. Journal of Petrology 55 (12), 2347–2376. doi:10.1093/petrology/egu059

Zack, T., & John, T., 2007. An evaluation of reactive fluid flow and trace element mobility in subducting slabs. Chemical Geology 239 (3–4), 199–216. doi:10.1016/j.chemgeo.2006.10.020

949 **Captions**

950 **Figure 1**

951

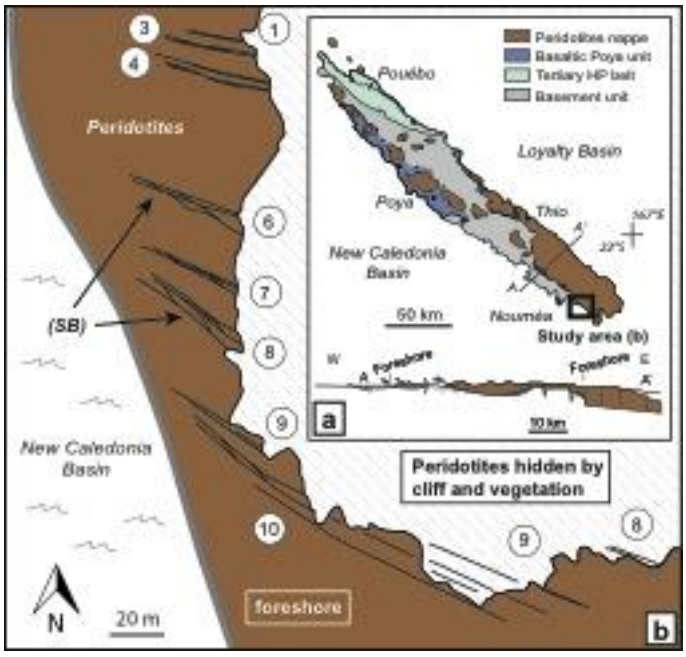

952

953 a) Simplified geological map and cross-section of New Caledonia Island (after Cluzel
954 et al., 2001); b) Structural map of the study area near to Plum Beach (S.E. of
955 Nouméa) showing the distribution of m-scale shear mafic bands within the peridotite
956 of the ophiolite. Shear band (SB) #2 is not represented at this scale.

957

958

Figure 2

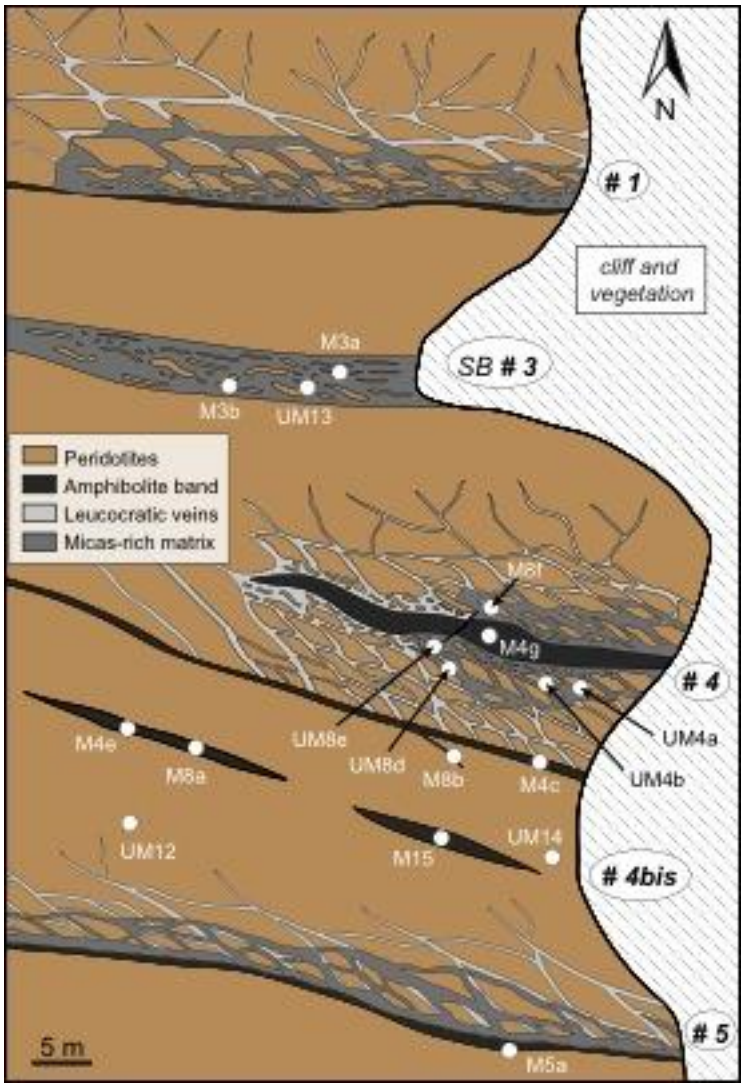

Structural map of the northern shear bands. Fig. 2 schematizing the relations between shear bands within the undeformed peridotite of the ophiolite. White dotes indicate sample location (Table 1). Shear band (SB) #2 is not represented at this scale.

Figure 3

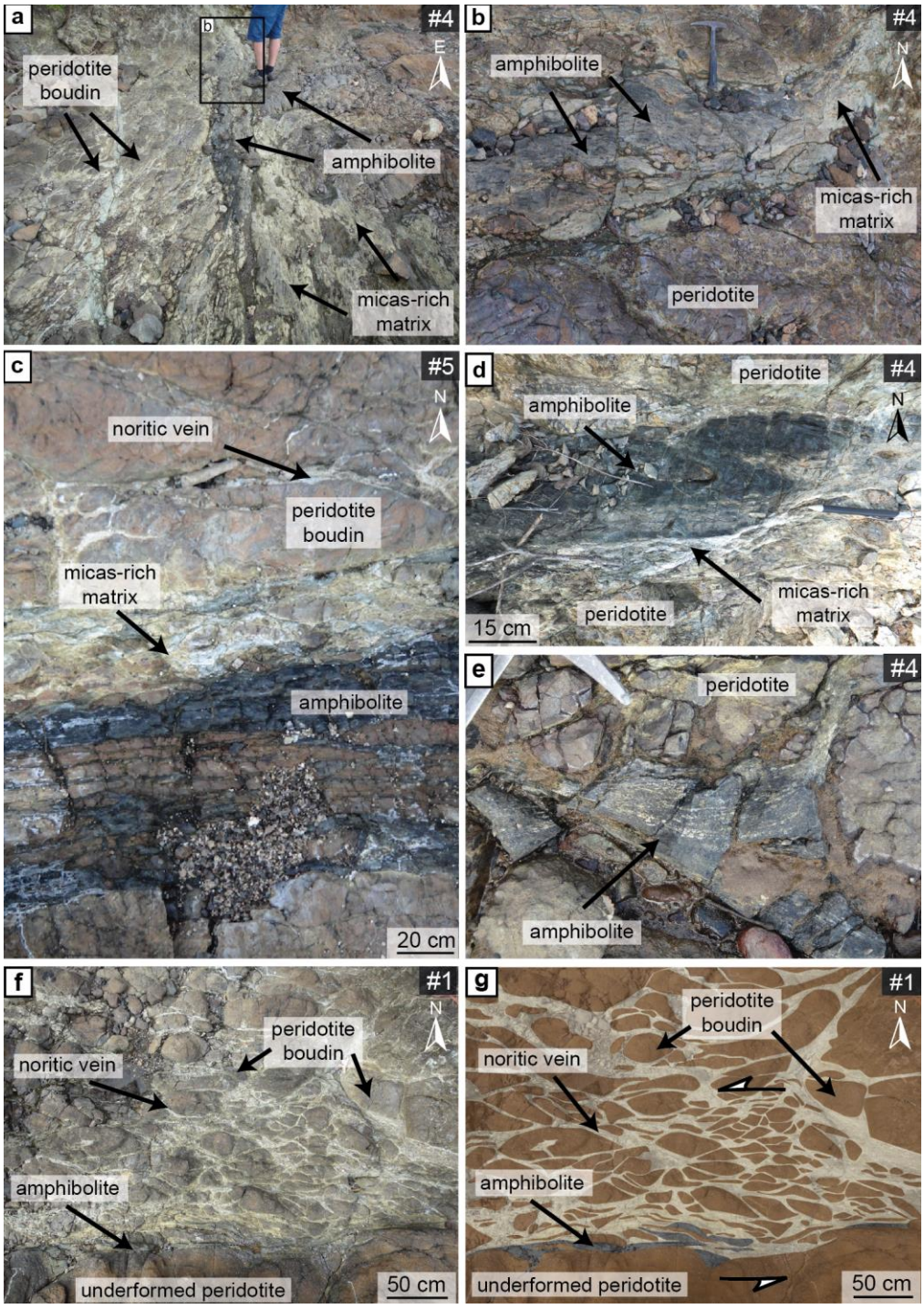

Structures of the mafic shear bands. Note that peridotite is highly boudinaged near dark dm-scale amphibolite bands. a) Amphibolite band found at the core of shear band #4. b) A small-scale amphibolite band cut by the major amphibolite #4. c) Shear band #5 is asymetrical. The vein network is developed only on one side of the

974 amphibolite band (to the NE). d) and e) Boudinaged and foliated amphibolite. f) and
975 g) Photograph and corresponding schematized sketch of asymmetrical shear band #1.
976 Vein density, thickness and length decrease away from the amphibolites.
977

Figure 4

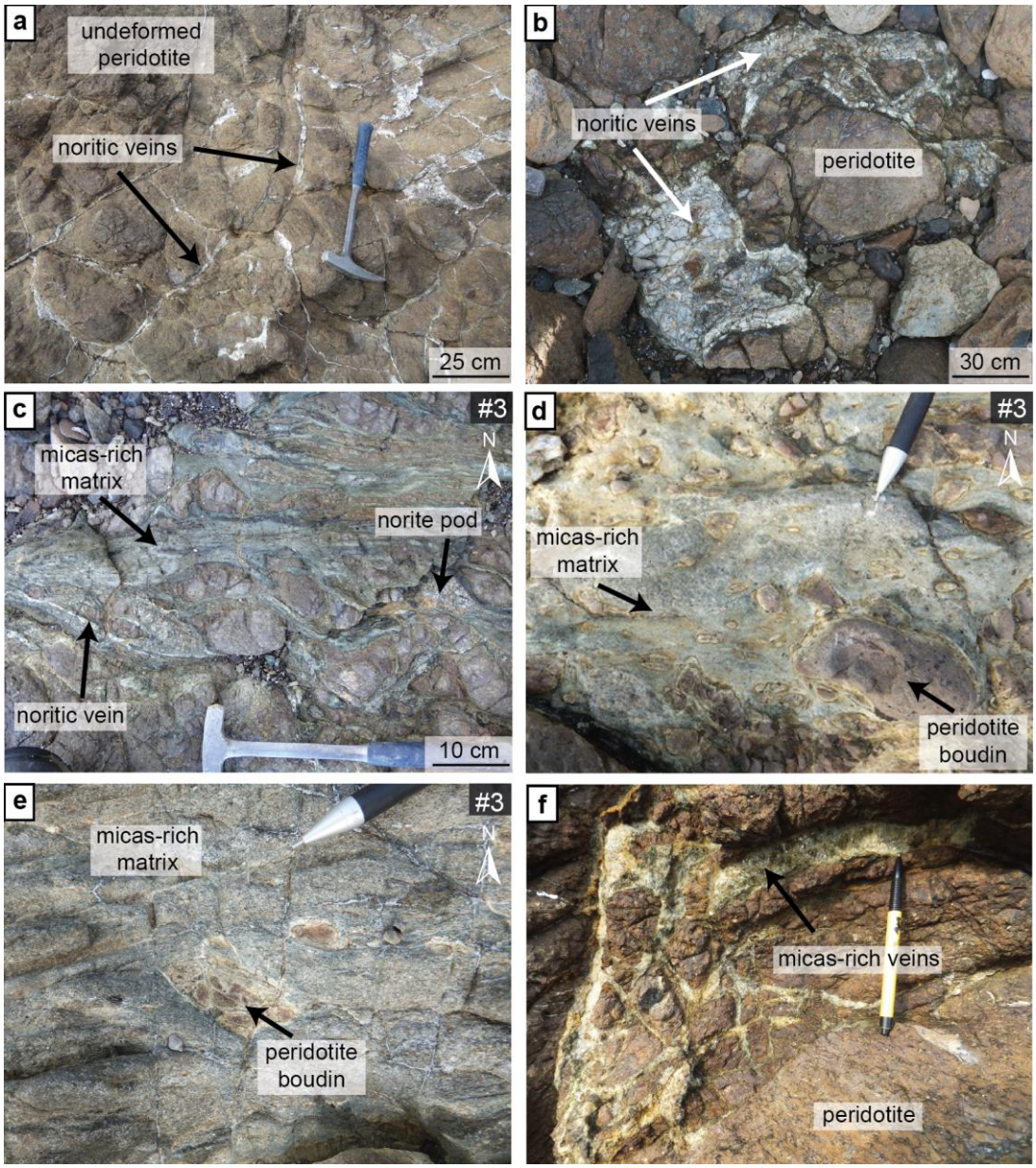

Photographs of the peridotite and the micas-rich matrix within and away from shear bands. a) and b) Weakly deformed feldspar-rich veins within undeformed peridotites away from shear bands. c), d), e) and f) Late light colored matrix with biotite, chlorite, talc and serpentine minerals within the shear bands. The matrix appears to form at the expense of both the mafic and ultramafic rocks.

Figure 5

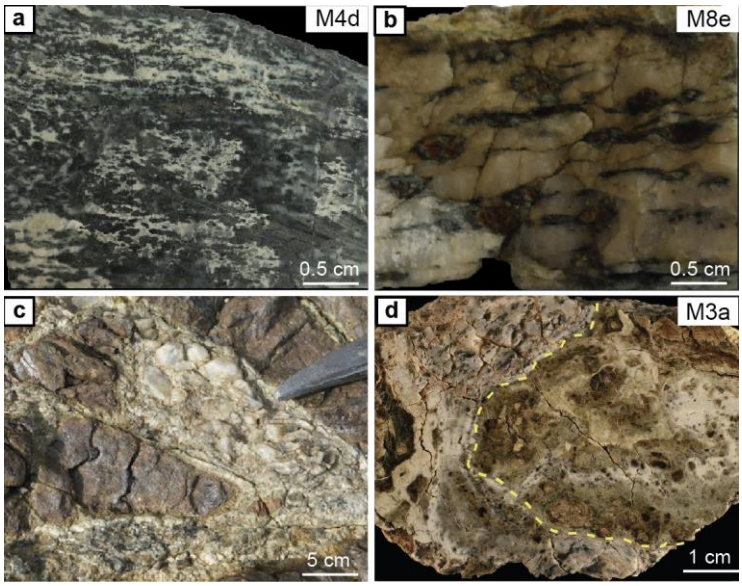

Representative samples of the different units observed in shear bands. a) Foliated amphibolite. White layers are mainly composed of plagioclase, darker layers contains amphibole and orthopyroxene. b) Feldspar-rich veins with brown coarse-grained orthopyroxene rimed by green amphiboles. c) Feldspar-rich vein wrapping around a peridotite boudin. Note the serpentine-bearing white rim around the boudin. d) Peridotite boudin wrapped by feldspar-rich vein and cross-cut by serpentine- talc-chlorite-rich white veinlets.

Figure 6

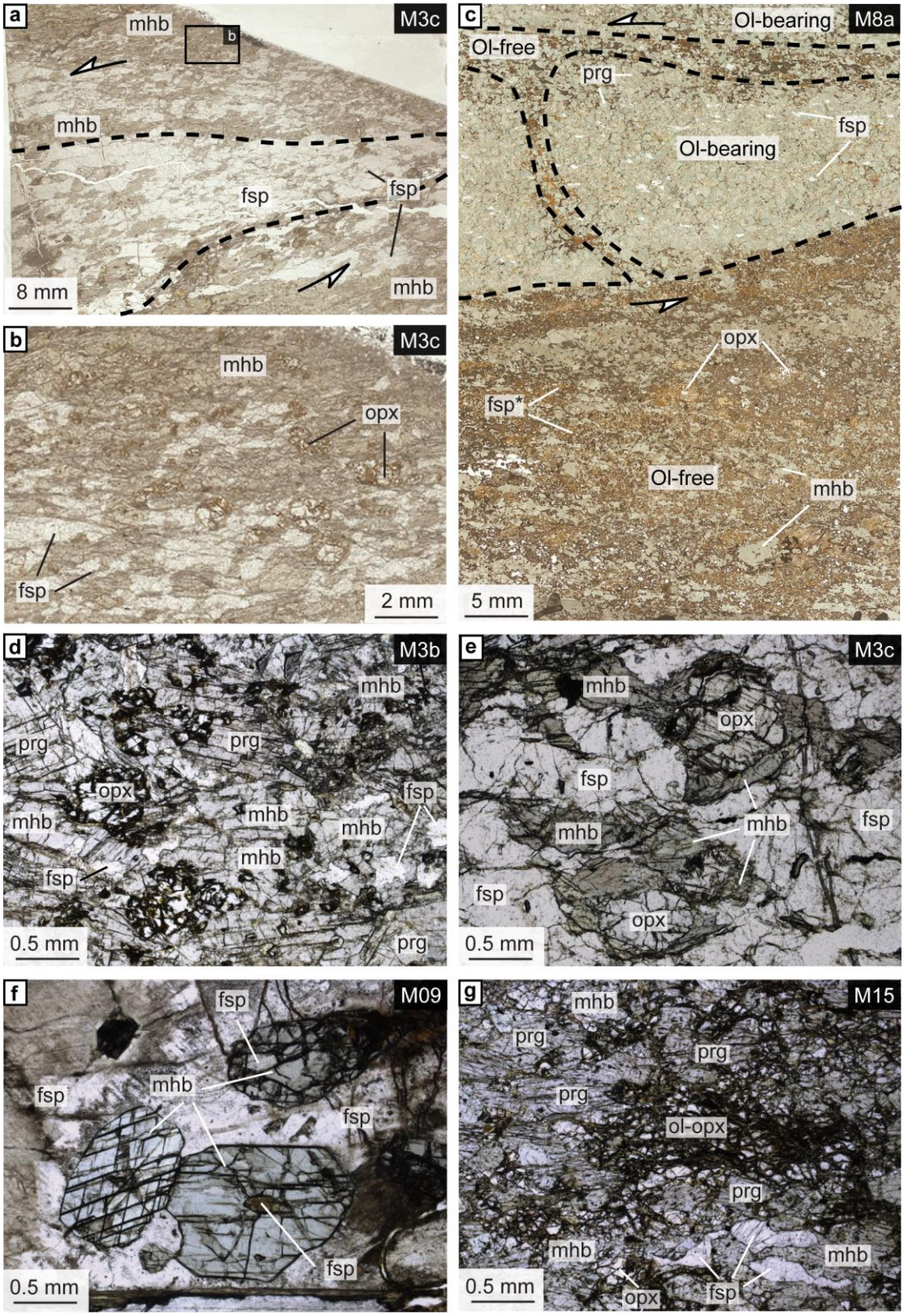
a
M3c
mhb
b
mhb
fsp
fsp
8 mm
mhb
b
M3c
mhb
opx
fsp
2 mm
c
Ol-bearing
M8a
Ol-free
prg
fsp
Ol-bearing
opx
fsp*
Ol-free
mhb
5 mm
d
M3b
mhb
prg
prg
opx
fsp
mhb
mhb
mhb
mhb
fsp
0.5 mm
prg
e
M3c
mhb
opx
fsp
mhb
mhb
fsp
fsp
opx
0.5 mm
f
M09
fsp
fsp
mhb
fsp
fsp
0.5 mm
g
M15
mhb
prg
prg
prg
ol-opx
prg
mhb
mhb
opx
fsp
0.5 mm

Representative mineral assemblages in amphibolite dikes. a) Olivine-free amphibolite with a boudinaged feldspar-rich layer within a hornblende-rich matrix. b) Zoom into the hornblende-rich matrix showing the destabilization of orthopyroxene. c) Pale olivine-bearing amphibolite band boudinaged and cross-cut by an olivine-free amphibolite layer. d) e) Assemblage of orthopyroxenes and plagioclases destabilized by the growth of amphiboles. f) Euhedral blue-pale amphibole growing in feldspar-rich vein away from deformation. g) Olivine, orthopyroxene and plagioclase boudinaged and destabilized by the syn-cinematic growth of amphibole. Abbreviations after Whitney and Evans (2010).

1009 **Figure 7**

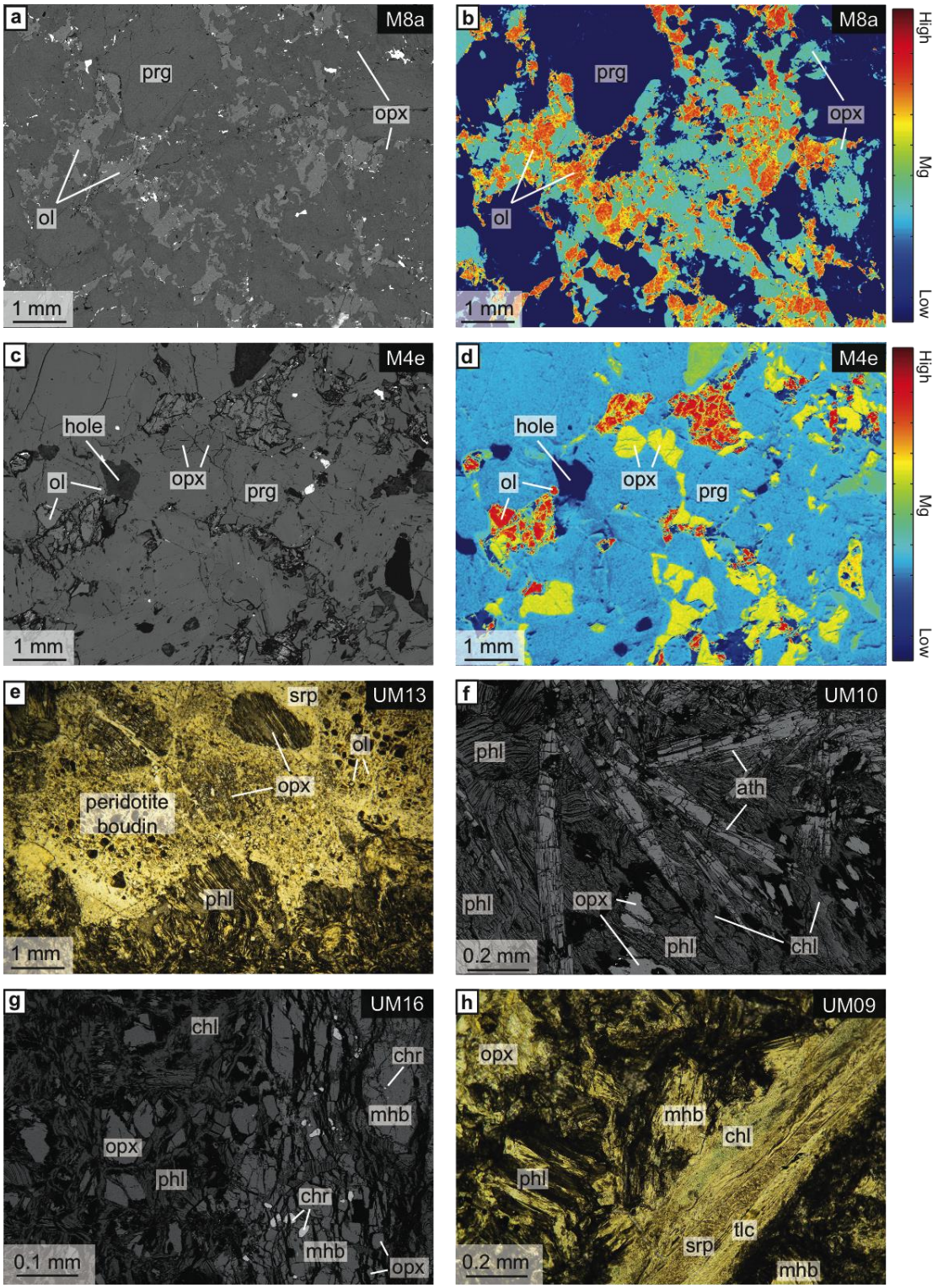

1010

1011 Representative mineral assemblages in olivine-bearing amphibolite and in micas-rich
1012 matrix. a), b), c) and d) Olivine and plagioclase destabilized by orthopyroxene and
1013 then amphibole. a) and c) are SEM back-scattered electron images, b) and d) are

corresponding SEM abundancy maps for Mg, where relative concentration is scaled on the right-end side color bar. e) and f) Microphotograph and SEM back-scattered electron image of peridotites boudins destabilized by the phlogopite-rich matrix associated to the anthophyllitic amphiboles. g) Coarse-grained hornblende pseudomorphing orthopyroxene and partially destabilized by phlogopite. h) Phlogopite-rich matrix cross-cut by veins of talc, chlorite and serpentine. Abbreviations after Whitney and Evans (2010).

Figure 8

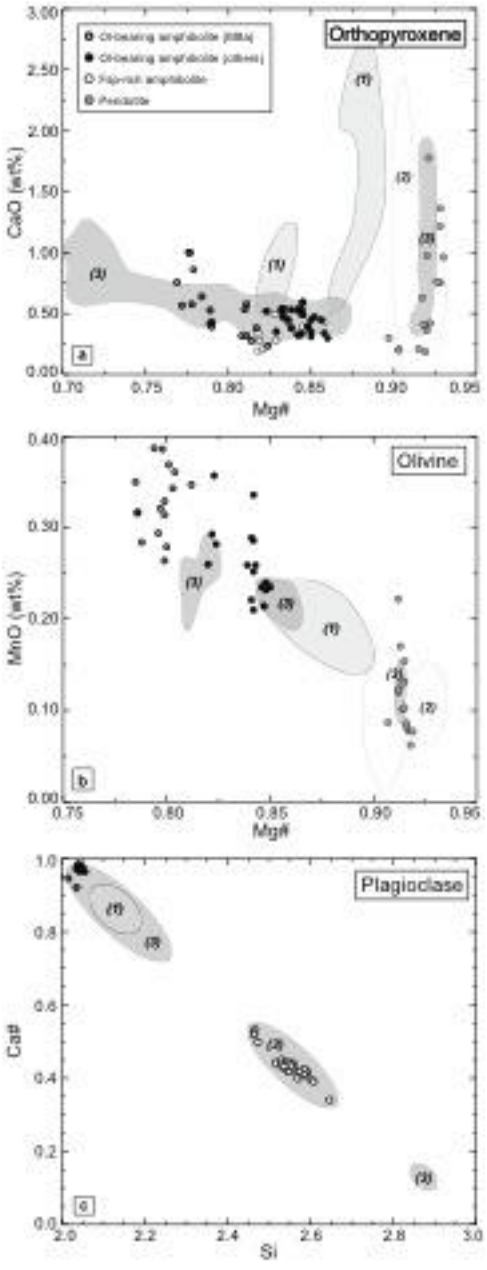

EPMA composition of selected minerals. a) Mg# [Mg/(Mg+Fe)] vs. CaO (wt%) in mafic and ultramafic orthopyroxene. b) Mg# vs. MnO (wt%) in mafic and ultramafic olivine. c) Si (p.f.u) vs. Ca# [Ca/(Ca+Na)] in plagioclase. (1) Gabbronorite sills (crustal cumulates; Pirard et al., 2013) ; (2) Peridotites from Massif du Sud (Marchesi et al., 2009) (3) Horblendite and amphibolite dikes (Pirard, 2012).

Figure 9

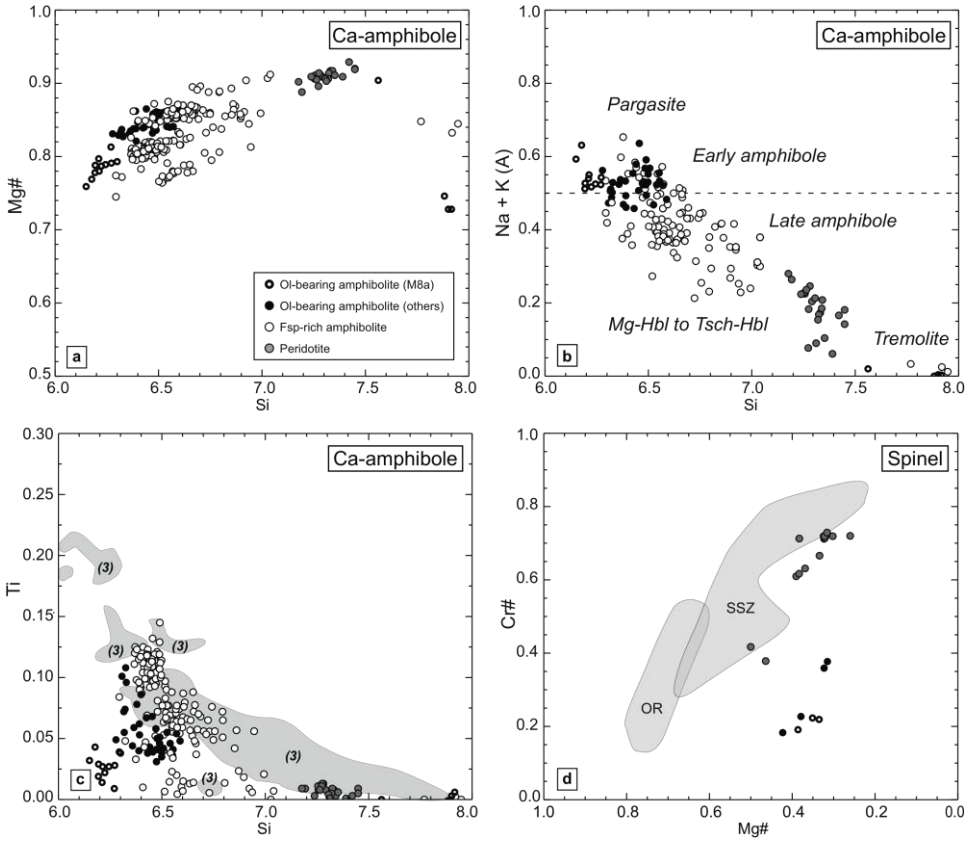

EPMA composition of amphibole and spinel in selected samples. a) Si (p.f.u) vs. Mg# in Ca-amphibole. b) Si (p.f.u) vs. $(Na+K)_A$ in Ca-amphibole after the classification of Leake et al. (1997). The dash line separates the pargasite domain (early amphibole) from the Mg-hornblende to tsch-horblende domains (late amphibole). c) Si (p.f.u) vs Ti (p.f.u) in Ca-amphibole. d) Mg# vs. Cr# in spinel. Or: Ocean ridge domain. SSZ: suprasubduction domain. (3) Horblendite and amphibolite dikes (Pirard, 2012)

Figure 10

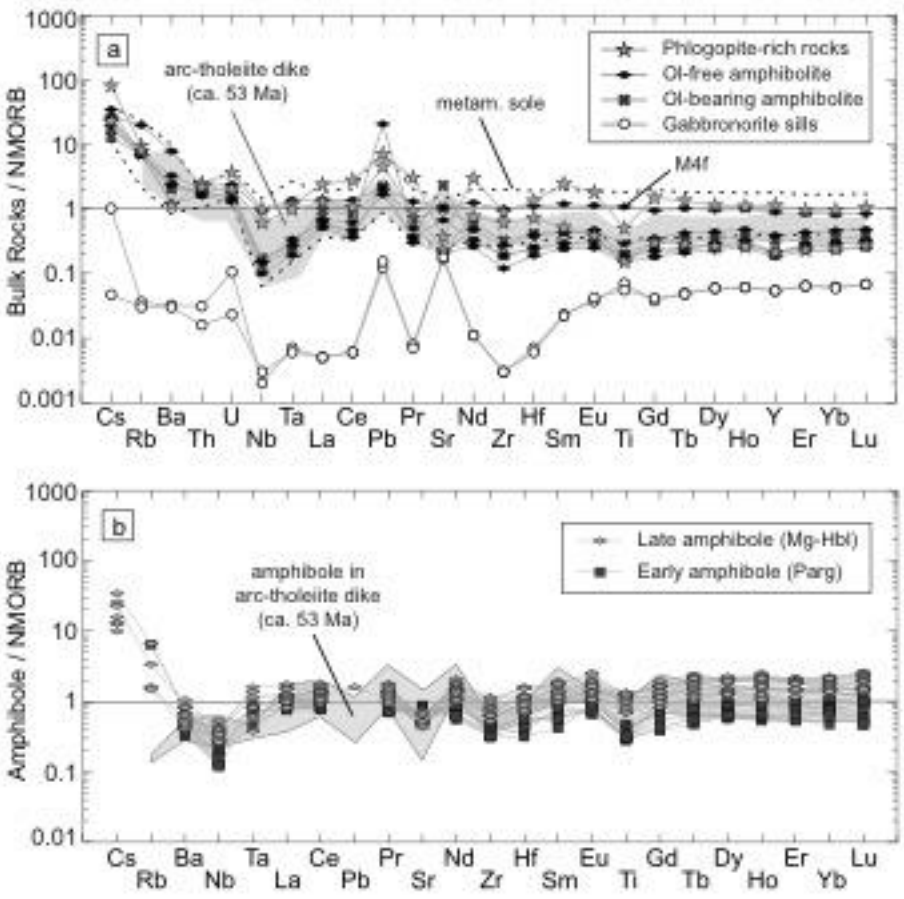

(a) Trace elements concentrations of amphibolite. The N-MORB normalization values are from Sun and Mcdonough (1989). Data for the metamorphic sole are from Cluzel et al. (2012) and for pre-obduction dikes (53 Ma) from Cluzel et al. (2006). Gabbronorite sills from the crustal cumulates are from Pirard et al. (2013). (b) Trace elements spider-diagrams of hornblende in olivine-free and olivine-bearing amphibolite M8a. Normalization values for the NMORB are from Sun and Mcdonough (1989). Grey area represents the trace elements values for amphibole in hornblendite and diorite dikes described by Pirard (2012).

Figure 11

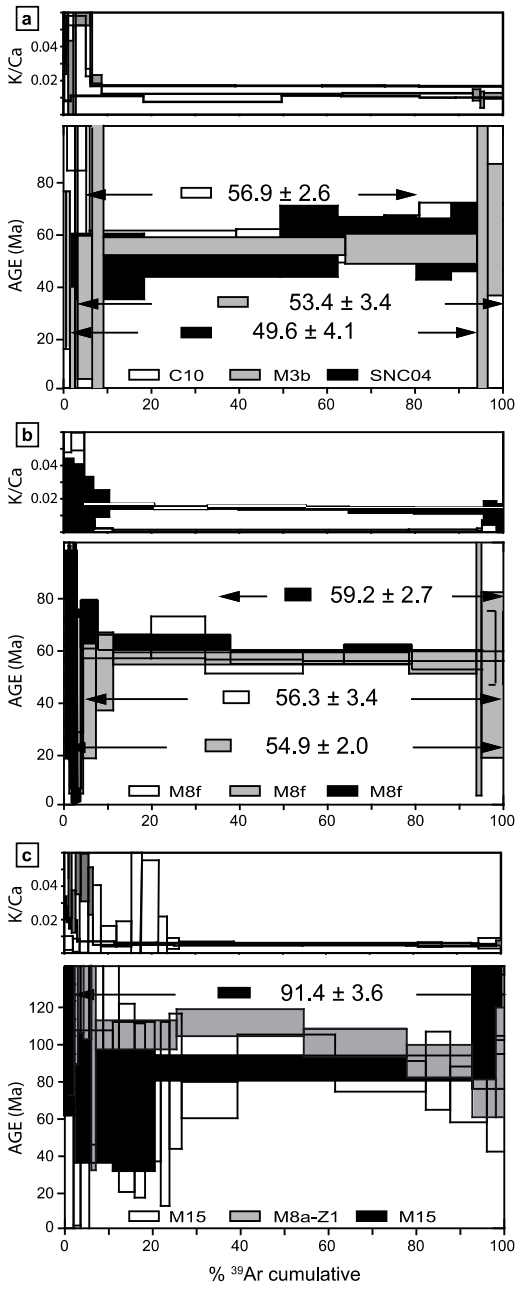

Representative $^{40}Ar/^{39}Ar$ age spectra of amphibole where K/Ca and calculated age are plotted as function of the cumulative fraction of ^{39}Ar released. Samples: C10: metamorphic sole sampled of Thio; SNC04: undeformed gabbroic dikes cross-cutting the Massif du Sud ophiolite; M8a-Z1 and M15: olivine-bearing; M8f and M3b: olivine-free amphibolite. Corresponding reverse isochron plots ($^{36}Ar/^{40}Ar$ vs. $^{39}Ar/^{40}Ar$) with intercept age are reported in the Online Fig. S1.

Figure 12

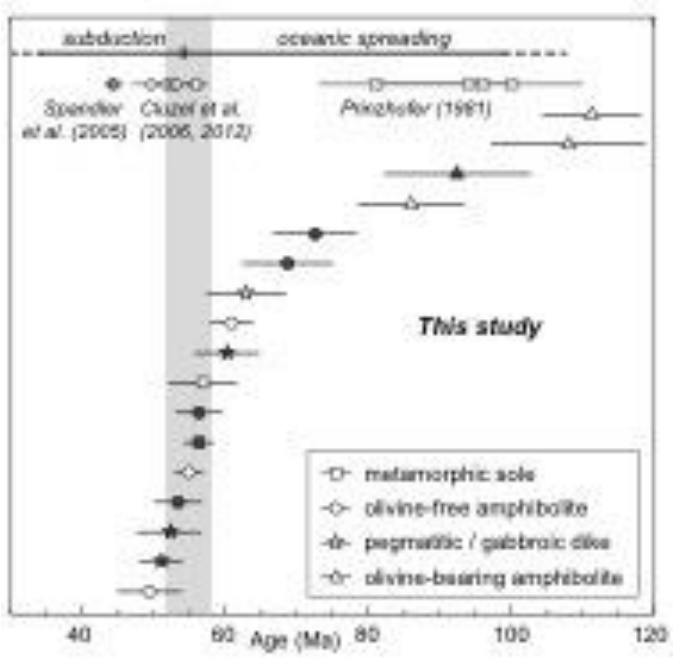

Plots of $^{40}Ar/^{39}Ar$ plateau age on amphibole from the different mafic units of the New Caledonia ophiolite in comparison of the timing of intrusion of pre-obduction dikes from Cluzel et al. (2006) and the metamorphic sole is from Cluzel et al. (2012). High-pressure rocks are from Spandler et al. (2005) and Cretaceous gabbroic dikes cross-cutting the peridotite are from Prinzhofer (1981). White-colored data are for $^{40}Ar/^{39}Ar$ plateau ages. Black-colored data are for $^{40}Ar/^{39}Ar$ preferred ages (plateau age or intercept age). See also Table 5.

Figure 13

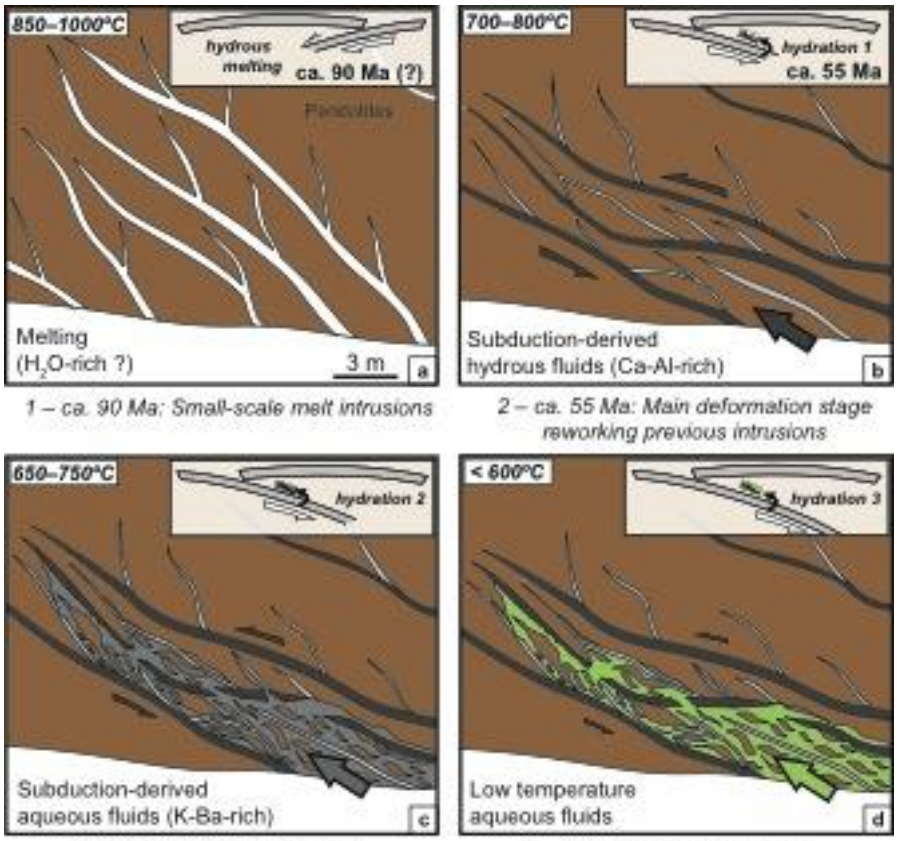

Schematized crystallization and deformation events for the emplacement of the mafic dikes at the study area scale. The inset shows the corresponding simplified geodynamic evolution with successive stages of infiltration of subduction-related fluids. a) Small-scale melt intrusions, enriched in Ca and Al compared to the surrounding harzburgites. Fluids at the origin of these mafic veins (with orthopyroxene, olivine, plagioclase ± early amphibole) were probably gabbroic melts derived from hydrated melting of the peridotite, caused by slab dehydration. b) Amphibolitization stage is the main deformation stage reworking previous mafic intrusions mechanically weaker than the peridotite host. Sheared amphibolites indicate that these mafic intrusions were deformed shortly after emplacement, as suggested by amphibole ages at 55 ± 2 Ma. c) The following emplacement of the phlogopite-rich matrix records the main metasomatic stage. Anthophyllite indicates

temperature around 700 ºC. The intensity of deformation decreased significantly compared to b). d) Talc–chlorite–serpentine assemblage representing the last stage of metasomatism affecting the shear bands and likely starting around temperatures of 600 ºC.

Online appendix

Figure S1

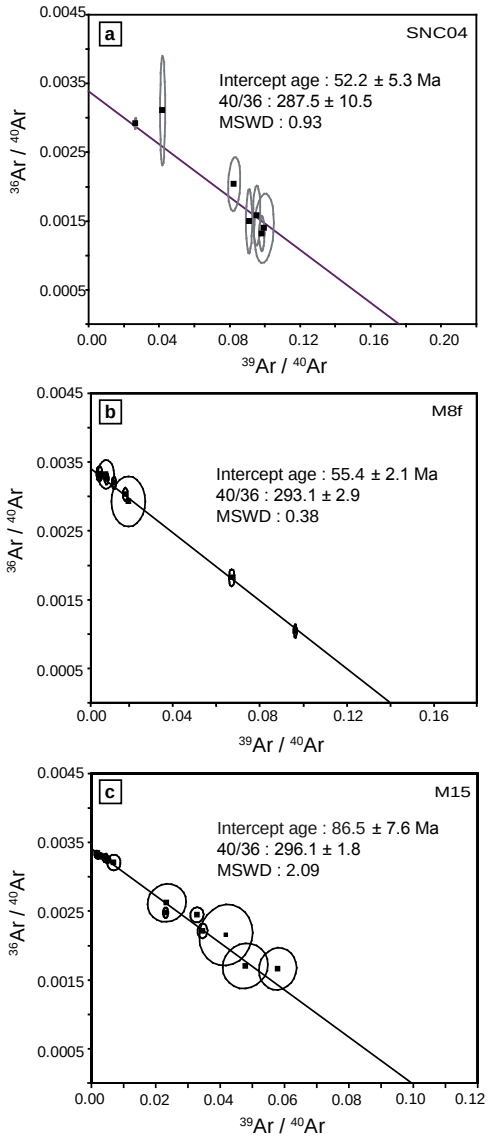

Corresponding reverse isochron plots ($^{36}Ar/^{40}Ar$ vs. $^{39}Ar/^{40}Ar$) are shown for some of the measurements, with intercept age, $^{36}Ar/^{40}Ar$ ratio and final reduced chi square (MSWD). Samples: SNC04: undeformed gabbroic dikes cross-cutting the Massif du Sud ophiolite; M15: olivine-bearing amphibolite; M8f and M3b: olivine-free amphibolite.

Tables

Table 1: Mineral occurrence for selected samples.

Unit	Sample	ol	opx	fsp	Ba-fsp	hbl	ath	phl	chl/tlc	srp
Undeformed peridotite	M12	x	x							l
	M14	x	x							l
Peridotite boudin	M9	x	x	v			o	o	l	l
	M10	x	x	v	o	o	o	o	l	l
	M16	x	x	v		o	o	o	l	l
Ol-bearing amphibolite	M8a	x	x	x		o			l	
	M8b	x	x	x		o			l	
	M4e	x	x	x		o				
	M15	x	x	x		o				
Ol-free amphibolite	M3c		x	x		o				
	M3b		x	x		o				
	M4c		x	x		o				
	Mx		x	x		o				
	M4d		x	x		o		l	l	
	M4g		x	x		o		l	l	
	8e		x	x		o				

x: primary phases, o: secondary phases; l: late phases; v: vein wrapping peridotite boudin. Mineral abreviations after Whitney and Evans (2010). Ba-fsp: celsian.

Table 2: Selected representative EPMA analyses for olivine, orthopyroxene, plagioclase and amphibole. Fe3+ for amphibole calculated after Leake et al. (1997)

Min.	Olivine				Min.	Orthopyroxene							
Samp.	M4e	M8a1	M8b	UM10	Samp.	M3c	M4e	M8a1	M8a2	M8b	M8e	UM10	UM16
SiO2	40.05	39.56	40.24	41.62	SiO2	55.85	55.02	54.51	54.69	56.04	55.86	57.44	58.08
TiO2	*b.d.l*	*b.d.l*	*b.d.l*	*b.d.l*	TiO2	*b.d.l*	*b.d.l*	*b.d.l*	*b.d.l*	*b.d.l*	0.12	*b.d.l*	*b.d.l*
Al2O3	*b.d.l*	*b.d.l*	*b.d.l*	*b.d.l*	Al2O3	1.34	2.12	1.88	1.23	1.60	1.55	1.50	0.70
Cr2O3	*b.d.l*	*b.d.l*	*b.d.l*	*b.d.l*	Cr2O3	*b.d.l*	*b.d.l*	0.08	*b.d.l*	0.07	*b.d.l*	0.72	0.09
FeO	14.25	18.31	16.12	8.14	FeO	11.12	10.00	13.74	14.78	10.85	10.38	5.24	6.69
MnO	0.23	0.28	0.36	0.08	MnO	0.23	0.25	0.49	0.42	0.28	0.25	0.08	0.11
MgO	45.46	41.73	43.11	50.38	MgO	31.24	32.28	28.76	28.13	30.26	31.78	34.94	34.89
CaO	*b.d.l*	*b.d.l*	*b.d.l*	*b.d.l*	CaO	0.28	0.47	0.53	0.57	0.54	0.39	0.42	0.20
Na2O	*b.d.l*	*b.d.l*	*b.d.l*	*b.d.l*	Na2O	*b.d.l*	*b.d.l*	*b.d.l*	*b.d.l*	*b.d.l*	*b.d.l*	*b.d.l*	*b.d.l*
K2O	*b.d.l*	*b.d.l*	*b.d.l*	*b.d.l*	K2O	*b.d.l*	*b.d.l*	*b.d.l*	*b.d.l*	*b.d.l*	*b.d.l*	*b.d.l*	*b.d.l*
BaO	*n.a*	*n.a*	*n.a*	*n.a*		*n.a*	*n.a*	*n.a*	*n.a*	*n.a*	*n.a*	*n.a*	*n.a*
Sum	100.0	99.9	99.8	100.2	Total	100.1	100.1	100.0	99.8	99.7	100.3	100.3	100.8
Formula unit													
Si	1.00	1.01	1.02	1.01	Si	1.96	1.92	1.94	1.96	1.98	1.95	1.97	1.99
Ti	0.00	0.00	0.00	0.00	Ti	0.00	0.00	0.00	0.00	0.00	0.00	0.00	0.00
Al	0.00	0.00	0.00	0.00	Al	0.06	0.09	0.08	0.05	0.07	0.06	0.06	0.03
Cr	0.00	0.00	0.00	0.00	Cr	0.00	0.00	0.00	0.00	0.00	0.00	0.02	0.00
Fe 3+	0.00	0.00	0.00	0.00	Fe 3+	0.02	0.08	0.03	0.02	0.00	0.02	0.00	0.00
Fe 2+	0.30	0.39	0.34	0.00	Fe 2+	0.31	0.21	0.38	0.42	0.32	0.28	0.15	0.19
Mn	0.00	0.01	0.01	0.17	Mn	0.01	0.01	0.01	0.01	0.01	0.01	0.00	0.00
Mg	1.70	1.59	1.63	0.00	Mg	1.64	1.68	1.53	1.50	1.60	1.66	1.78	1.78
Ca	0.00	0.00	0.00	1.82	Ca	0.01	0.02	0.02	0.02	0.02	0.01	0.02	0.01
Na	0.00	0.00	0.00	0.00	Na	0.00	0.00	0.00	0.00	0.00	0.00	0.00	0.00
K	0.00	0.00	0.00	0.00	K	0.00	0.00	0.00	0.00	0.00	0.00	0.00	0.00
Ba	-	-	-	-	Ba	-	-	-	-	-	-	-	-
Mg#	0.85	0.80	0.83	0.92	Mg#	0.83	0.85	0.79	0.77	0.83	0.85	0.92	0.90

b.d.l: below detection limit; n.a.: non analyzed

1113

Table 2: Selected representative EPMA analyses for olivine, orthopyroxene, plagioclase and amphibole. Fe3+ for amphibole calculated after Leake et al. (1997)

Min.	Olivine				Min.	Orthopyroxene								Min.	Feldspar				
Samp.	M4e	M8a1	M8b	UM10	Samp.	M3c	M4e	M8a1	M8a2	M8b	M8e	UM10	UM16	Samp.	M8a1	M8a1	M8e	UM9	UM10
SiO2	40.05	39.56	40.24	41.62	SiO2	55.85	55.02	54.51	54.69	56.04	55.86	57.44	58.08	SiO2	43.24	43.55	56.68	56.62	51.19
TiO2	*b.d.l*	*b.d.l*	*b.d.l*	*b.d.l*	TiO2	*b.d.l*	*b.d.l*	*b.d.l*	*b.d.l*	*b.d.l*	0.12	*b.d.l*	*b.d.l*	TiO2	*b.d.l*	*b.d.l*	*b.d.l*	*b.d.l*	*b.d.l*
Al2O3	*b.d.l*	*b.d.l*	*b.d.l*	*b.d.l*	Al2O3	1.34	2.12	1.88	1.23	1.60	1.55	1.50	0.70	Al2O3	37.18	36.77	27.62	26.70	22.52
Cr2O3	*b.d.l*	*b.d.l*	*b.d.l*	*b.d.l*	Cr2O3	*b.d.l*	*b.d.l*	0.08	*b.d.l*	0.07	*b.d.l*	0.72	0.09	Cr2O3	*b.d.l*	*b.d.l*	*b.d.l*	*b.d.l*	*b.d.l*
FeO	14.25	18.31	16.12	8.14	FeO	11.12	10.00	13.74	14.78	10.85	10.38	5.24	6.69	FeO	*b.d.l*	*b.d.l*	*b.d.l*	*b.d.l*	*b.d.l*
MnO	0.23	0.28	0.36	0.08	MnO	0.23	0.25	0.49	0.42	0.28	0.25	0.08	0.11	MnO	*b.d.l*	*b.d.l*	*b.d.l*	*b.d.l*	*b.d.l*
MgO	45.46	41.73	43.11	50.38	MgO	31.24	32.28	28.76	28.13	30.26	31.78	34.94	34.89	MgO	*b.d.l*	*b.d.l*	*b.d.l*	*b.d.l*	*b.d.l*
CaO	*b.d.l*	*b.d.l*	*b.d.l*	*b.d.l*	CaO	0.28	0.47	0.53	0.57	0.54	0.39	0.42	0.20	CaO	20.33	19.40	9.13	9.48	0.13
Na2O	*b.d.l*	*b.d.l*	*b.d.l*	*b.d.l*	Na2O	*b.d.l*	*b.d.l*	*b.d.l*	*b.d.l*	*b.d.l*	*b.d.l*	*b.d.l*	*b.d.l*	Na2O	0.21	0.54	6.47	6.61	0.46
K2O	*b.d.l*	*b.d.l*	*b.d.l*	*b.d.l*	K2O	*b.d.l*	*b.d.l*	*b.d.l*	*b.d.l*	*b.d.l*	*b.d.l*	*b.d.l*	*b.d.l*	K2O	*b.d.l*	*b.d.l*	*b.d.l*	*b.d.l*	7.92
BaO	*n.a*	*n.a*	*n.a*	*n.a*		*n.a*	*n.a*	*n.a*	*n.a*	*n.a*	*n.a*	*n.a*	*n.a*	BaO	*n.a*	*n.a*	*n.a*	*n.a*	15.78
Sum	100.0	99.9	99.8	100.2	Total	100.1	100.1	100.0	99.8	99.7	100.3	100.3	100.8	Sum	101.0	100.3	99.9	99.4	98.0
Formula unit																			
Si	1.00	1.01	1.02	1.01	Si	1.96	1.92	1.94	1.96	1.98	1.95	1.97	1.99	Si	1.98	2.00	2.46	2.54	2.65
Ti	0.00	0.00	0.00	0.00	Ti	0.00	0.00	0.00	0.00	0.00	0.00	0.00	0.00	Ti	0.00	0.00	0.00	0.00	0.00
Al	0.00	0.00	0.00	0.00	Al	0.06	0.09	0.08	0.05	0.07	0.06	0.06	0.03	Al	2.00	1.99	1.52	1.42	1.37
Cr	0.00	0.00	0.00	0.00	Cr	0.00	0.00	0.00	0.00	0.00	0.00	0.02	0.00	Cr	0.00	0.00	0.00	0.00	0.00
Fe 3+	0.00	0.00	0.00	0.00	Fe 3+	0.02	0.08	0.03	0.02	0.00	0.02	0.00	0.00	Fe 3+	0.00	0.00	0.00	0.00	0.00
Fe 2+	0.30	0.39	0.34	0.00	Fe 2+	0.31	0.21	0.38	0.42	0.32	0.28	0.15	0.19	Fe 2+	0.00	0.00	0.00	0.00	0.00
Mn	0.00	0.01	0.01	0.17	Mn	0.01	0.01	0.01	0.01	0.01	0.01	0.00	0.00	Mn	0.00	0.00	0.00	0.00	0.00
Mg	1.70	1.59	1.63	0.00	Mg	1.64	1.68	1.53	1.50	1.60	1.66	1.78	1.78	Mg	0.00	0.00	0.00	0.00	0.03
Ca	0.00	0.00	0.00	1.82	Ca	0.01	0.02	0.02	0.02	0.02	0.01	0.02	0.01	Ca	1.00	0.95	0.53	0.46	0.01
Na	0.00	0.00	0.00	0.00	Na	0.00	0.00	0.00	0.00	0.00	0.00	0.00	0.00	Na	0.02	0.05	0.48	0.58	0.05
K	0.00	0.00	0.00	0.00	K	0.00	0.00	0.00	0.00	0.00	0.00	0.00	0.00	K	0.00	0.00	0.00	0.00	0.36
Ba	-	-	-	-	Ba	-	-	-	-	-	-	-	-	Ba	-	-	-	-	0.52
Mg#	0.85	0.80	0.83	0.92	Mg#	0.83	0.85	0.79	0.77	0.83	0.85	0.92	0.90	Ca#	0.98	0.95	0.52	0.44	0.13

Table 2 (continued)

Min.	Amphibole													
Samp.	M3c	M3c	M8a1	M8a1	M8a2	M8b	M8e	M8e	M09	UM10	UM10	UM10	UM16	UM16
	mhb	mhb	prg	tr	mhb	prg	mhb	mhb	mhb	mhb	tr	ath	mhb	tr
SiO2	47.08	45.41	43.33	55.40	46.30	46.11	46.04	49.96	46.99	48.13	53.96	57.08	51.52	54.23
TiO2	0.19	1.01	0.40	*b.d.l*	0.79	0.39	0.06	0.06	0.68	0.44	0.07	*b.d.l*	*b.d.l*	*b.d.l*
Al2O3	11.10	11.47	15.16	3.14	11.82	12.24	11.54	8.42	11.66	10.58	5.73	1.57	8.44	4.76
Cr2O3	*b.d.l*	*b.d.l*	*b.d.l*	*b.d.l*	0.10	0.44	*b.d.l*	*b.d.l*	*b.d.l*	0.85	*b.d.l*	0.05	*b.d.l*	*b.d.l*
FeO	7.03	7.38	8.20	4.16	8.85	6.11	7.20	6.32	5.86	4.09	3.51	9.14	3.83	3.05
MnO	0.18	0.05	0.10	0.12	0.09	0.08	0.15	0.17	0.09	0.06	0.04	0.26	0.05	0.12
MgO	18.26	17.64	15.27	21.91	16.08	17.47	17.55	19.28	18.88	19.62	21.81	28.58	20.97	22.41
CaO	11.51	11.27	12.03	12.73	11.71	12.35	11.38	11.29	11.52	11.72	12.06	0.73	12.02	11.90
Na2O	2.20	2.50	2.80	0.53	2.13	2.38	2.47	1.82	2.20	2.48	1.26	0.12	1.67	1.09
K2O	0.12	0.15	0.10	*b.d.l*	0.06	0.07	0.13	0.08	0.13	0.14	0.05	*b.d.l*	0.08	*b.d.l*
Sum	97.67	96.89	97.38	97.99	97.94	97.63	96.51	97.41	98.04	98.11	98.50	97.51	98.58	97.56
Si	6.57	6.41	6.18	7.56	6.52	6.49	6.51	6.94	6.52	6.66	7.33	7.77	7.03	7.42
Ti	0.02	0.11	0.04	0.00	0.08	0.42	0.01	0.01	0.07	0.05	0.01	0.00	0.00	0.00
Al	1.83	1.90	2.55	0.51	1.96	2.03	1.92	1.38	1.90	1.73	0.92	0.25	0.97	0.77
Cr	0.00	0.00	0.00	0.00	0.01	0.05	0.00	0.00	0.00	0.09	0.00	0.01	0.00	0.00
Fe 3+	0.82	0.87	0.55	0.47	0.70	0.48	0.85	0.73	0.68	0.47	0.40	0.17	0.35	0.44
Fe 2+	0.00	0.00	0.43	0.00	0.34	0.24	0.00	0.00	0.00	0.00	0.00	0.87	0.00	0.00
Mn	0.02	0.01	0.01	0.01	0.00	0.01	0.02	0.02	0.01	0.01	0.01	0.03	0.01	0.01
Mg	3.70	3.72	3.24	0.46	3.37	3.66	3.70	3.99	3.90	4.05	4.42	5.80	4.57	4.26
Ca	1.72	1.71	1.84	1.86	1.77	1.86	1.73	1.68	1.71	1.74	1.76	0.11	1.75	1.76
Na	0.60	0.69	0.78	0.14	0.58	0.65	0.68	0.49	0.59	0.66	0.33	0.03	0.29	0.44
K	0.02	0.03	0.02	0.00	0.01	0.01	0.02	0.02	0.02	0.02	0.01	0.00	0.01	0.00
Mg#	0.82	0.81	0.77	0.49	0.76	0.84	0.81	0.84	0.86	0.90	0.92	0.85	0.93	0.91
Geothermobarometry after Holland and Blundy (1994) modified by Anderson and Smith (1995)														
An#	0.52	0.52	0.95	-	0.52	0.52	0.52	0.52	0.44	0.44	-	-	0.44	-
T (˚C)	718	776	1013	-	756	963	739	702	680	677	-	-	615	-
P (kbar)	5.16	4.33	error	-	4.98	error	5.23	3.34	5.97	3.61	-	-	3.78	-

Table 3: Whole rock geochemistry for representative amphibolite dikes.

Sample	M15_Z1 amph	M4f amph	M15_Z2 ol-amph	M8a ol-amph	M4e ol-amph	M4a amph(1)	M4g amph(1)
SiO2 (wt %)	43.83	49.45	43.61	44.66	43.09	46.96	45.81
TiO2	0.38	1.38	0.00	0.26	0.24	0.19	0.64
Al2O3	7.41	14.09	9.35	10.41	8.94	7.29	10.13
Fe2O3	9.59	9.78	11.10	8.12	9.89	5.88	5.59
MnO	0.18	0.15	0.17	0.14	0.15	0.07	0.08
MgO	21.54	8.12	20.99	20.30	25.40	25.86	21.90
CaO	7.65	9.71	8.25	9.21	7.03	2.60	8.56
Na2O	1.42	3.96	1.70	1.80	1.61	1.53	1.61
K2O	*b.d.l.*	0.74	*b.d.l.*	0.02	*b.d.l.*	0.10	0.07
P2O5	0.03	0.13	0.03	0.06	0.03	0.02	0.03
Perte 1000	6.41	1.52	3.16	4.72	3.54	9.47	5.21
Sum	98.43	99.03	98.60	99.69	99.91	99.78	99.00
Cr (ppm)	960.00	336.00	1249.00	1652.00	2212.00	1140.00	802.00
Ni	348.00	94.00	523.00	544.00	819.00	922.00	648.00
Cs	0.14	0.19	0.17	0.12	0.09	0.16	0.56
Rb	3.90	11.10	4.00	4.00	3.90	4.40	5.30
Ba	20.70	49.40	14.90	12.80	15.10	*n.d*	7.10
Th	0.25	0.27	0.22	0.22	0.21	0.26	0.30
U	0.09	0.11	0.07	0.08	0.07	0.09	0.17
Nb	0.37	2.24	0.34	0.40	0.31	1.42	2.28
Ta	0.04	0.18	0.05	0.04	0.03	0.13	0.16
La	1.76	3.49	1.53	2.37	1.39	3.19	5.96
Ce	4.56	10.26	3.48	6.16	3.29	8.03	20.82
Pb	6.19	0.62	0.50	0.66	0.64	1.36	2.12
Pr	0.66	1.72	0.49	0.90	0.46	1.22	4.01
Sr	19.40	95.60	60.60	91.80	208.50	20.90	33.60
Nd	3.45	9.07	2.42	4.20	2.25	5.44	21.72
Zr	20.00	74.00	14.00	24.00	14.00	45.00	65.00
Hf	0.80	2.30	0.51	0.84	0.49	1.50	2.72
Sm	1.14	3.13	0.76	1.17	0.72	1.33	6.45
Eu	0.48	1.15	0.33	0.43	0.30	0.39	1.84
Gd	1.27	3.45	0.83	1.11	0.75	1.10	5.44
Tb	0.28	0.68	0.17	0.22	0.16	0.19	0.90
Dy	2.00	4.39	1.30	1.53	1.21	1.18	5.11
Ho	0.48	1.00	0.32	0.37	0.29	0.26	1.10
Y	11.00	25.00	6.00	9.00	6.00	6.00	32.00
Er	1.29	2.51	0.83	0.97	0.78	0.68	2.80
Yb	1.39	2.48	0.90	1.07	0.87	0.74	2.94
Lu	0.22	0.38	0.15	0.17	0.14	0.12	0.47

(1) mafic amphibolite altered by 1- the phlogopite-rich matrix and 2- late chlorite-rich matrix
b.d.l: below detection limit

1114

Table 4:: LA-ICP-MS geochemistry for representative Ca-amphibole in amphibolite dikes.

Sample	M8a1	M8a1	M8a1	M8a2	M8a2	M8a2
Mineral	prg	prg	prg	mhb	mhb	mhb
SiO2 (wt%)	43.12	45.46	43.98	48.14	43.82	46.32
TiO2	0.30	0.09	0.21	0.53	0.77	0.85
Al2O3	13.99	12.79	14.11	10.48	13.13	11.82
Cr2O3	0.07	0.15	0.24	0.17	0.10	0.07
FeO	8.97	6.53	7.85	7.70	9.29	8.76
MnO	0.16	0.07	0.10	0.13	0.08	0.06
MgO	15.84	17.43	16.28	16.80	15.24	16.10
CaO	11.83	12.37	12.12	11.64	11.89	12.01
Na2O	2.79	2.39	2.44	1.82	2.48	2.14
K2O	0.07	0.04	0.05	0.04	0.07	0.07
Sum	97.13	97.31	97.37	97.47	96.87	98.20
Cs (ppm)	*b.d.l.*	*b.d.l.*	*b.d.l.*	*b.d.l.*	0.24	0.07
Rb	*b.d.l.*	*b.d.l.*	*b.d.l.*	*b.d.l.*	3.72	b.d.l.
Ba	2.18	2.05	2.77	2.68	5.21	3.79
Nb	0.36	0.31	0.40	0.68	0.65	0.87
Ta	*b.d.l.*	*b.d.l.*	*b.d.l.*	*b.d.l.*	0.11	0.15
La	2.23	1.90	2.26	2.57	2.67	2.81
Ce	6.31	5.76	6.63	7.95	7.09	9.64
Pb	*b.d.l.*	*b.d.l.*	*b.d.l.*	*b.d.l.*	*b.d.l.*	*b.d.l.*
Pr	0.95	0.92	1.23	1.60	1.21	1.67
Sr	73.11	68.75	67.36	41.47	46.78	48.35
Nd	4.05	4.59	5.67	7.81	8.66	10.30
Zr	24.49	23.12	30.51	48.31	38.45	56.43
Hf	1.13	0.85	1.04	1.95	1.62	2.08
Sm	1.50	b.d.l.	1.64	3.23	2.96	2.74
Eu	0.87	0.76	0.81	1.08	1.09	1.46
Gd	*b.d.l.*	1.41	3.34	3.10	3.62	6.02
Tb	0.33	0.32	0.62	0.82	0.69	1.20
Dy	2.76	2.86	3.86	5.97	6.50	8.42
Ho	0.67	0.68	0.93	1.31	1.18	2.03
Er	2.36	1.60	2.80	4.20	3.43	5.65
Yb	2.26	1.44	2.53	4.72	4.13	5.58
Lu	0.22	0.36	0.49	0.62	0.67	0.76

See appendix for spider diagrams.

Abreviations after Whitney and Evans (2010)

1115

Table 5: $^{40}Ar/^{39}Ar$ age performed on amphiboles from mafic dikes cross-cutting the peridotite of the New Caledonia ophiolite.

Sample	Lithology	Location	Total fusion age	Plateau age	$\%^{39}Ar$	Intercept age	$(^{40}Ar/^{36}Ar)_i$	MSWD	Preferred age	38Ar/37Ar	38Ar/39Ar
C10 (1)	MS amphibolite	Thio	59.12 ± 2.24	56.21 ± 2.14	95.6	*nd*	*nd*	*nd*	56.21 ± 2.14	*nd*	*nd*
C10 (2)	MS amphibolite	Thio	68.23 ± 2.97	56.85 ± 4.79	96.0	*nd*	*nd*	*nd*		*nd*	*nd*
SNC01 (1)	Pegmatite dike	Massif du Sud	53.67 ± 3.14	60.20 ± 4.62	92.5	*nd*	*nd*	*nd*	60.20 ± 4.62	0.011	0.41
SNC01 (2)	Pegmatite dike	Massif du Sud	87.66 ± 5.94	62.87 ± 5.54	61.8	*nd*	*nd*	*nd*		0.01	0.36
SNC03 (1)	Gabbro	Massif du Sud	51.13 ± 4.49	51.25 ± 3.12	81.5	51.32 ± 4.18	295.7 ± 21.1	0.65	51.25 ± 3.12	0.013	0.53
SNC04 (1)	Gabbro	Massif du Sud	47.59 ± 4.36	49.56 ± 3.98	97.8	52.22 ± 5.34	287.5 ± 10.5	0.93	52.22 ± 5.34	0.007	0.27
M3b (1)	ol-free amphibolite	Plum beach	53.64 ± 4.27	53.35 ± 3.39	78.0	54.10 ± 3.40	293.6 ± 5.0	1.25	54.10 ± 3.40	0.005	0.18
M4d (1)	ol-free amphibolite	Plum beach	238.54 ± 7.50	/	/	/	/	/		0.02	1.72
M4d (2)	ol-free amphibolite	Plum beach	73.10 ± 5.49	68.67 ± 6.37	97.4	67.59 ± 5.06	303.7 ± 5.0	1.02	67.59 ± 5.06	0.02	1.73
M8f (1)	ol-free amphibolite	Plum beach	58.34 ± 3.61	56.29 ± 3.28	95.8	52.86 ± 5.34	318.6 ± 20.6	1.79	56.23 ± 4.42	*nd*	*nd*
M8f (2)	ol-free amphibolite	Plum beach	62.08 ± 2.61	60.82 ± 3.06	92.2	60.25 ± 2.84	299.6 ± 4.2	1.77		0.004	0.11
M8f (3)	ol-free amphibolite	Plum beach	93.78 ± 3.08	49.34 ± 4.47	49.31	56.46 ± 7.40	282.5 ± 12.1	0.23		0.004	0.07
M8f (4)	ol-free amphibolite	Plum beach	53.43 ± 2.85	54.86 ± 2.04	99.5	55.36 ± 2.11	293.1 ± 2.9	0.38		0.003	0.08
M8a-Z1 (1)	ol-bearing amphibolite	Plum beach	107.69 ± 7.09	107.94 ± 10.80	67.7	92.81 ± 13.43	349.1 ± 19.0	1.56		0.017	1.71
M8a-Z1 (2)	ol-bearing amphibolite	Plum beach	125.24 ± 4.51	111.22 ± 6.93	70.8	92.50 ± 11.65	351.7 ± 3.7	1.28	92.50 ± 11.65	0.017	1.68
M8a-Z2 (1)	ol-free amphibolite	Plum beach	76.61 ± 7.31	72.54 ± 5.83	86.1	73.85 ± 6.74	297.0 ± 9.6	1.55	73.85 ± 6.74	0.024	1.87
M15 (2)	ol-bearing amphibolite	Plum beach	81.80 ± 4.20	/	/	/	/	/		0.019	1.59
M15 (3)	ol-bearing amphibolite	Plum beach	89.97 ± 8.42	85.94 ± 7.50	87.9	86.54 ± 7.58	296.1 ± 1.8	2.09		0.017	1.28
M15 (4)	ol-bearing amphibolite	Plum beach	167.09 ± 21.48	/	/	/	/	/	/	0.013	1.74

Preferred age is determined after plateau age, intercept age or a mean of different analysis for a same sample when the plateau age is not significant.

MS: metamorphic sole; MSWD: mean square weighted deviation.